Perovskite-related ReO_3 structures: A diverse family, from oxides to metal-organic frameworks.

Hayden A. Evans,[1,2] Yue Wu,[3] Ram Seshadri,[1,4,5] & Anthony K. Cheetham[1,5,6]

[1]*Materials Research Laboratory, University of California, Santa Barbara*

California 93106 United States.

[2]*National Institute of Standards and Technology, Center for Neutron Research*

Gaithersburg, Maryland 20899, United States.

[3]*University of Liverpool, Department of Chemistry and Materials Innovation Factory*

Crown Street, Liverpool, L69 7ZD, Merseyside, England, U.K.

[4]*Department of Chemistry and Biochemistry, University of California, Santa Barbara*

California 93106 United States.

[5]*Materials Department, University of California, Santa Barbara*

California 93106 United States

[6]*Department of Materials Science and Engineering, National University of Singapore*

Singapore 117575, Singapore

Correspondence email: hayden.evans@nist.gov, akc30@cam.ac.uk

ORCID HAE 0000-0002-1331-4274; YW 0000-0003-2874-8267;

RS 0000-0001-5858-4027; AKC 0000-0003-1518-4845

Abstract

ReO_3-type structures can be described as ABX_3 perovskites in which the *A*-cation site is unoccupied. They therefore have the general composition BX_3, where *B* is normally a cation and *X* is a bridging anion. The chemical diversity of such structures is very broad, ranging from simple oxides and fluorides, such as WO_3 and AlF_3, to more complex systems in which the bridging anion is polyatomic, as in the Prussian blue-related cyanides such as $Fe(CN)_3$ and $CoPt(CN)_6$. The same topology is also found in metal-organic frameworks, for example $In(Im)_3$ (Im = imidazolate), and even the well-known MOF-5 structure, where the *B*-site cation is itself polyatomic. This remarkable chemical diversity gives rise to a wide range of interesting and often unusual properties, including negative thermal expansion (ScF_3), photocatalysis ($CoSn(OH)_6$), thermoelectricity ($CoAs_3$), and even a report of superconductivity in a phase that is controversially described as SH_3 with a doubly interpenetrating ReO_3 structure. We present a comprehensive account of this exciting family of materials and discuss current challenges and future opportunities in the area.

1 Introduction

Recent developments in photovoltaic devices with active layers containing hybrid perovskite halides such as $(MA)PbI_3$ (MA = methylammonium)[1] have drawn our attention once more to the importance and versatility of perovskite-based materials. These iconic materials, of general formula AMX_3 [Figure 1(a)], have a long and distinguished his-

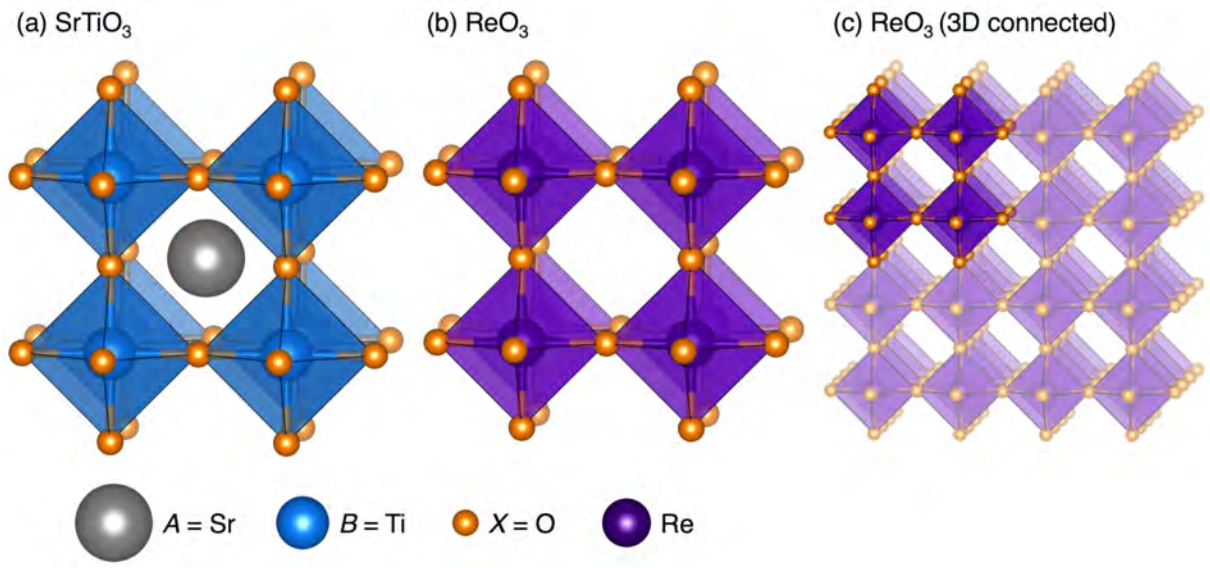

Figure 1: (a) The ABX_3 perovskite structure, exemplified by cubic $SrTiO_3$; (b) The ReO_3 structure, illustrated by ReO_3 itself, contains no cation on the *A*-site. It is therefore an array of corner-sharing BX_6 octahedra. These figures are drawn to scale to remind the reader that the ReO_3 unit cell is smaller due to the smaller size of the Re^{6+} cation; (c) The ReO_3 structure, drawn to show its extended connectivity. The VESTA software suite was used to create all visualizations of crystal structures in this manuscript.[9]

tory, with major milestones including the discoveries of ferroelectric $BaTiO_3$,[2] ferromagnetic $SrRuO_3$,[3] superconducting $YBa_2Cu_3O_7$,[4] magnetoresistive (La/Sr)MnO_3,[5] and multiferroic $BiMnO_3$.[6] Striking breakthroughs in the hybrid perovskite area include the discoveries of ferroelectric and multiferroic behaviour in formates such as (DMA)$Mn(HCOO)_3$, (DMA = dimethylammonium), where the *X* anion is an organic linker rather than a simple halide or oxide anion,[7] and the ferroelectric, metal-free perovskites ((N-methyl-N'-diazabicyclo[2.2.2]octonium)-ammonium triiodides) that were recently reported.[8]

It is often forgotten, however, that the ABX_3 perovskite structure is itself based on an even simpler structure type in which there are no cations in the *A*-site cavities. Such BX_3-

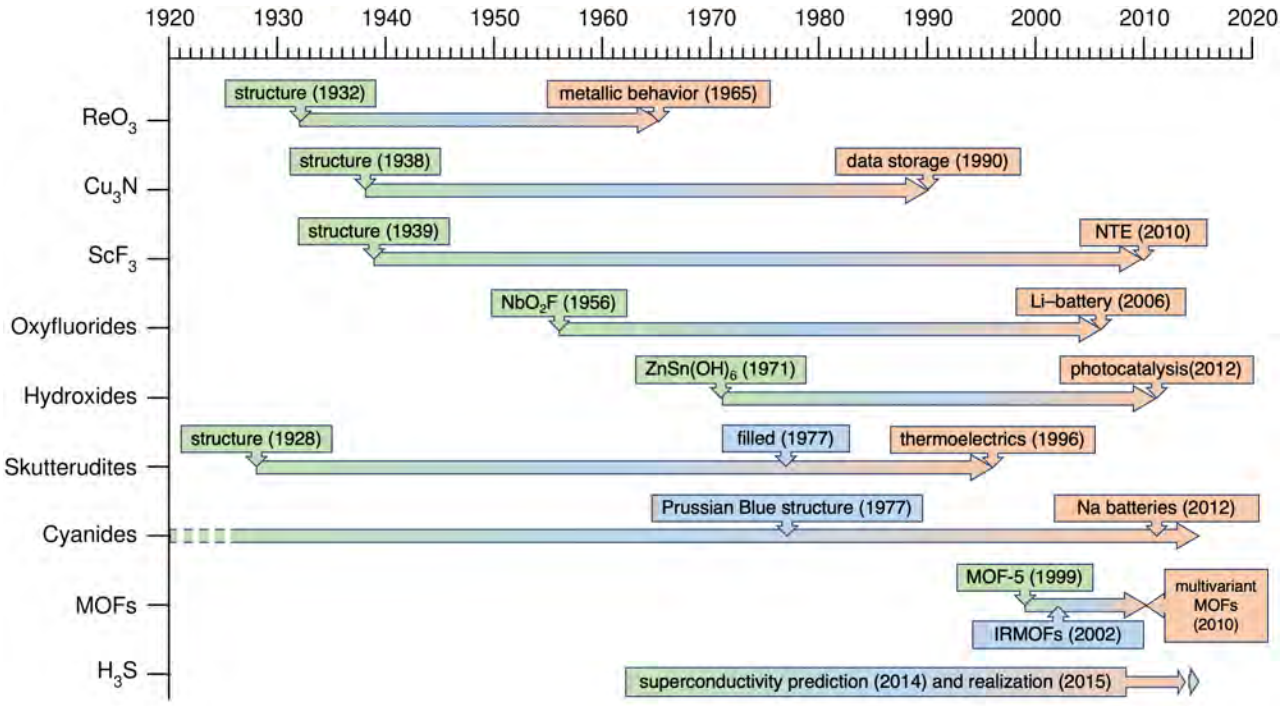

Figure 2: Timeline of ReO_3-type compounds. It is interesting to note the long period between discoveries and reported properties, as well as the diverse chemical compositions and functionalities, of the ReO_3-type materials.

type structures (these are typically MX_3 structures, where M is a metal) are most notably illustrated by the eponymous ReO_3 system, shown in Figure 1(b) and (c). It comprises a network of ReO_6 octahedra that share common corners in three dimensions, in this case with an Re–O–Re angle of 180° (though in general such linear linkages are unusual.) Recalling that the perovskite family now comprises an extensive range of systems with both simple and complex X anion linkers,[10] we have begun to explore the extent to which this is also true for ReO_3-type materials. Our article addresses this question, drawing together the many examples of ReO_3-type phases, ranging from simple oxides and halides, such as WO_3 and ScF_3, to systems containing more complex linkers and nodes, such as the formates $M^{III}(HCOO)_3$, hypophosphites $M^{III}(H_2POO)_3$, imidazolates $M^{III}(C_3N_2H_3)_3$, and borohydrides $Ln(BH_4)_3$. We shall show that this family is far more extensive than has hitherto been recognized, and that they display a remarkable range of functionality that almost matches that of the perovskites. Figure 2 illustrates this point, showing the timelines of discoveries and properties of these ReO_3-type materials, as well as their considerable chemical scope. Furthermore, our survey of the literature in this area suggests that there are several additional systems that have yet to be explored.

One of the characteristics of the ReO_3-type structures is their openness, which is immediately apparent when comparing ReO_3 itself with the perovskite structure in Figure 1. This feature is even more striking in expanded ReO_3 structures, such as those in which the X-site has a multi-atom linker. There are several aspects of the openness that can have an important influence on both the structures and properties of ReO_3 systems. In

terms of the structures, the openness often results in tilting of the BX_6 octahedra, leading to more stable structures with bent *B*–*X*–*B* linkages.[11] Tilting of octahedra in perovskites has been extensively studied,[12–14] including the analysis of group-subgroup relationships, and the concepts in this area have recently been extended to multi-atom *X*-site linkers.[15,16] These well-established ideas can be equally applied to ReO_3-type structures but will not be discussed further here. However, we note that tilting, or the absence of it, can have a significant impact on electronic and magnetic properties, as will be seen in the case of ReO_3, itself, as well as in some of the cyanides. Turning to other manifestations of the openness of ReO_3-type structures, we note that cation insertion into the vacant *A*-site cavity is often facile, both in terms of the availability of space and the ease of ion transport; this has enabled a number of applications in the area of rechargeable batteries. The openness also amplifies the vibrational properties associated with the *X*-site linkers, which has led to some outstanding examples of negative thermal expansion. Finally, in the case of multi-atom *X*-site linkers, where the openness is particularly high, we shall find many examples of systems that can accommodate guest molecules in the *A*-site cavities, leading in some cases to interesting adsorption-desorption behaviour.

Our article begins with a focus on simple inorganic systems, especially the oxides, fluorides and oxyfluorides, and then explores more complex phases with multi-atom linkers on the *X*-site. Note that one of the requirements for the adoption of the ReO_3-type structure or topology is that the system must be able to support octahedral connectivity at the *B*-sites. Bearing this in mind, we shall also consider some metal-organic frameworks

(MOFs) in which the *B* site node is itself polyatomic, the most striking of which is the metal-organic framework, MOF-5.[17] The nomenclature for these materials in the MOF literature is quite varied and includes the use of the terms pcu (primitive cubic), α-plutonium and reo networks. For simplicity, we shall simply refer to them as ReO_3-type structures.

2 Inorganics

Oxides The oxide ReO_3, which is deep red in colour, was first reported in the early 1930's when its synthesis was described and the structure determined by powder X-ray diffraction.[18] However, it was not until 1965 when Goodenough and co-workers reported that it was a metallic conductor that it attracted the attention of the scientific community.[19] Oxide conductors were rarities at that time, and the behaviour of ReO_3 was particularly eye-catching because its conductivity was almost as high as that of copper metal. That finding led to subsequent studies of its electronic structure, which involves band formation from overlap between the rhenium 5d (t_{2g}) and O 2p ($p_{x/y}$) orbitals.[20] More than 50 years after the work of Goodenough, it remains the most striking example of a metallic transition metal oxide.

ReO_3 and WO_3 are the only binary oxides that crystallize with the ReO_3-type structure, but though structurally similar, they have properties that are quite different. For example, at room temperature, ReO_3 is primitive cubic and conductive, as described above, while WO_3 is monoclinic and insulating. The difference lies in their contrasting *M*–O–*M*

bond angles, where ReO_3 has angles of 180°, and WO_3 has angles of between 165° and 179°.[21] This distortion is due to the propensity for W atoms to off-center from the ideal cubic location location in the WO_6 octahedral environments, which density functional theory (DFT) calculations suggest is caused by non-populated antibonding orbitals in the conduction band. In ReO_3 it is the reverse, as the antibonding orbitals are populated and the off-centering is discouraged.[22] This theory has been supported by experiment, since solid solutions between ReO_3 and WO_3 ($Re_xW_{1-x}O_3$) become cubic at an x value of 0.25; this change is also marked by an increase in conductivity.[23]

ReO_3 and WO_3 also differ in that WO_3 undergoes multiple first-order phase transitions with temperature, whereas ReO_3 does not (the cubic ReO_3 structure is stable from liquid helium temperature to its 673 K melting point.)[24] However, ReO_3 does display negative thermal expansion (NTE).[24,25] NTE is the phenomenon where a material contracts instead of expanding when heated. This property proves useful in composites, where the strain from the positive thermal expansion (PTE) of one phase can be offset by the NTE of another.[26] Studies by Rodriquez *et al.* described how for ReO_3 samples with high static disorder of oxygen, NTE was diminished.[27] The weakened NTE is due to the oxygen disorder, which alters the state of the antibonding band, reducing the Fermi pressure responsible for the structure's rigidity. In a more holistic sense, NTE is commonly seen in materials with corner connected *M*–*X* tetrahedra or octahedra which undergo concerted tilting or rocking motions when transverse vibrations (the movement of *X* species perpendicular to the *M*–*X*–*M* bond) are excited.[28] Famous NTE compounds such as ZrW_2O_8, Prussian blues

and zeolites, all display some form of excited transverse vibrational modes related to their NTE behavior.[28] We shall see other striking examples of NTE in ReO_3-type systems in some of the following sections.

In addition to exhibiting NTE, ReO_3 displays pressure-induced first order phase transitions. These pressure dependent phase transitions (which involve octahedral rotations) occur as a stress relief,[29] as the ReO_6 octahedra do not distort easily because of the strong Re–O bonds.[30] The pressure induced phase transitions have been examined via diffraction experiments,[31–33] but only recently with the implementation of high pressure Raman studies was a clear pressure phase diagram resolved.[34] Outside of physical pressure, chemical pressure in the form of lithiation can also induce phase transitions in ReO_3, as was first examined in the 1980's by Cava *et al.*,[35,36] and more recently by Melot and co-workers,[37] where considerable correlated rotations of the corner-sharing ReO_6 octahedra are observed upon lithiation.

Lastly, though ReO_3 has generated a large amount of interest, it should not be overlooked that WO_3 is an attractive wide band gap semiconductor which can be tuned through intercalation, temperature, doping, and nano/microstructuring. Nano/microstructuring in particular, is quite attractive, as this can stabilize one of the three other WO_3 phases at room temperature,[38] or increase surface area for enhanced chemical functionality. For example, past work on WO_3 for its use as a photochromic,[39,40] electrochromic,[41] photocatalytic,[42] superconductive,[43] ferroelectric,[44] as well as a gas-sensing material,[45–48] is still quite rel-

evant, with most areas still the focus of active research.[49] Current work on WO_3, for example, ranges from photoelectrochemical,[50–54] photochromic,[55] conductive,[56] anodic,[57] photocatalytic,[58–61] thermoelectric,[62,63], and gas-sensing[64,65] applications, but there are some particularly interesting developments of late.

One recent work used WO_3 as an electron conductor in a core/shell nanowire $BiVO_4$ photoanode for photoelectrochemical water oxidation.[66] This was significant, as by utilizing this core/shell nanowire design the researchers overcame the low transport properties of $BiVO_4$ whilst still leveraging its high light absorption. Another recent example demonstrated how an apoferritin-encapsulated, nanoparticle coated, WO_3 material was capable of sensitive detection of certain molecules in exhaled breath, demonstrating great promise for reliable, non-invasive, diagnosis of diseases.[64] Lastly, recent work showed that WO_3 is able to tune the surface charge transfer of diamond.[67] In fact, the transfer doping efficiency with WO_3 was the highest per minimal surface acceptor coverage reported to date, marking a sizable advance in 2D diamond-based electronic devices. This recent work on WO_3, in combination with that of the past, attests to the wide variety of applications this material continues to have.

Nitrides The anti-ReO_3 crystal structure of Cu_3N was determined in 1938 by Juza and Hahn,[69] not long after the discovery of ReO_3 itself, and has been confirmed in more recent work.[70] Its crystal structure in space group $Pm\bar{3}m$ is the same as that of ReO_3, since the N–Cu–N bond angles are also 180°. Under high pressure, Cu_3N transforms to a simple

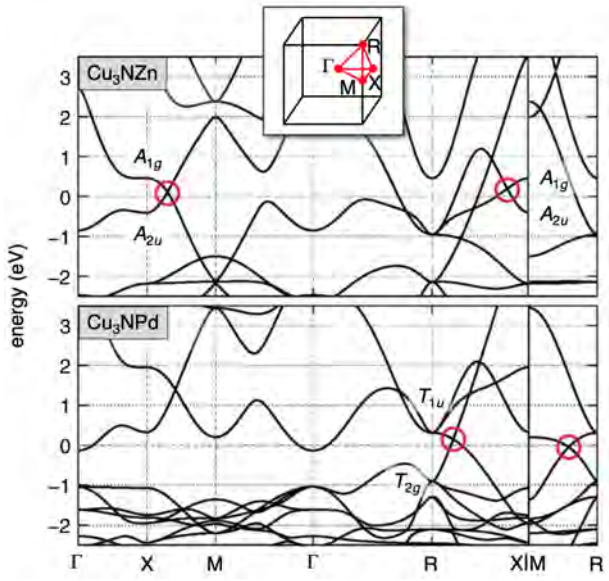

Figure 3: Electronic structures and Z_2 indices of (a) Cu_3NZn and (b) Cu_3NPd. Bands are drawn along the high-symmetry lines of the Brillouin zone (inset). The Dirac points are indicated by red circles. Parity eigenvalues are illustrated at the eight parity-invariant points in the first octant of the Brillouin zone. This figure and caption were reproduced with permission from Kim *et al.*[68]

tetragonal structure, which is not surprising given the open nature of the structure.[71] There has not been a detailed study of NTE in Cu_3N, but a recent report indicates that there is little, if any, expansion in the temperature range of 4 K – 100 K.[72] More than fifty years from its discovery elapsed before the growth of thin films was reported,[73] and attention was drawn to the interesting semiconducting properties of Cu_3N. Shortly afterwards, in 1990, it was shown that such films, which are typically green, could be used as an optical data recording medium using infrared light.[74] Since copper does not react directly with nitrogen gas, the films were made by irradiating copper with nitrogen ions during film deposition onto a substrate (though bulk samples can be made from the reaction between CuF_2 and NH_3).[75] Since 1990, there has been extensive work on the preparation of high quality thin

films by using a variety of methods, especially magnetron sputtering and RF plasma jets. In addition to its potential for optical data storage, Cu_3N has also been proposed as a defect-tolerant semiconductor for PV applications,[76] while in condensed matter physics it has been suggested as a model for a new type of topological semi-metal exhibiting Dirac line nodes near the Fermi energy on doping with nonmagnetic transition metal atoms, such as Zn and Pd (Figure 3).[68] In the energy storage area, Cu_3N has been studied as a potential cathode material for lithium ion batteries, though the chemistry is complex and may well preclude any real applications in this field.[77] It has also been studied as a potential cathode for oxygen reduction in alkaline fuel cells.[78]

Dark-blue sodium nitride, Na_3N, which is isostructural to Cu_3N, has been prepared by the reaction of metallic sodium or liquid Na-K alloy with plasma-activated nitrogen at low pressures.[79] Na_3N decomposes above 104° C into the elements, with ΔHf estimated at $+64(2)$ kJ/mol.[80] The band gap of Na_3N is in the range 0.5 eV – 1.0 eV, which is similar to that of Cu_3N. It shows no phase change down to 20 K, but does exhibit strongly anisotropic effects.[81] There is no tilting of the NNa_6 octahedra, nor is there any NTE, which is perhaps surprising. However, like Cu_3N, it does exhibit interesting topological semimetal behavior.[82] It is also worth noting that neither Li_3N nor K_3N adopt the anti ReO_3-type structure.[83,84]

Fluorides and Oxyfluorides ReO_3-type fluoride materials, of general formula MF_3, are more common than their oxide counterparts, owing in part to the greater prevalence of

3+ oxidation state metals. The *M*-site metals for MF_3 compounds include M = Sc,[85] Co,[86] Al,[87] Cr,[88] V,[89] Ti,[90] and Fe.[88] It is worth noting that rare-earth cations, even the smallest example of lutetium (ionic radius of 0.861 Å)[91,92], appear to be too large to adopt the octahedral coordination required for the ReO_3-type structure. The majority of the single metal ReO_3-type fluoride compounds adopt a rhombohedral distorted variant at room temperature, with the exceptions being ScF_3, a notable NTE material, and MnF_3, which is Jahn-Teller distorted.[85] As will become apparent throughout this review, the majority of inorganic ReO_3-type materials have been studied for properties that are exhibited by ReO_3 itself: curious thermal expansion, as a host for guest cations, and unusual structural behaviour with pressure. This does not mean, however, that they do not, or cannot, display other interesting properties.

In terms of MF_3 compounds, ScF_3 is perhaps the most well known as it displays a remarkable temperature range of NTE (linked to the transverse vibrations of the F anions).[93] From 10 K to approximately 1100 K,[94] the material does not undergo any first-order phase transitions (although a possible quantum phase transition has been reported[95]), and displays a coefficient of NTE near $-8\,\mathrm{ppm\,K^{-1}}$ at room temperature. This is comparable to $-9\,\mathrm{ppm\,K^{-1}}$ for the well known high performing NTE compound, ZrW_2O_8.[85] Furthermore, it was recently shown that the degree of NTE in ScF_3 is particle size dependent,[96] and can actually be tuned between NTE, zero thermal expansion (ZTE), and PTE, by nanostructuring the product.[97] The tunability has been ascribed to local symmetry breaking as the particle size is decreased, i.e. the local structure is rhombodrally distorted (as evi-

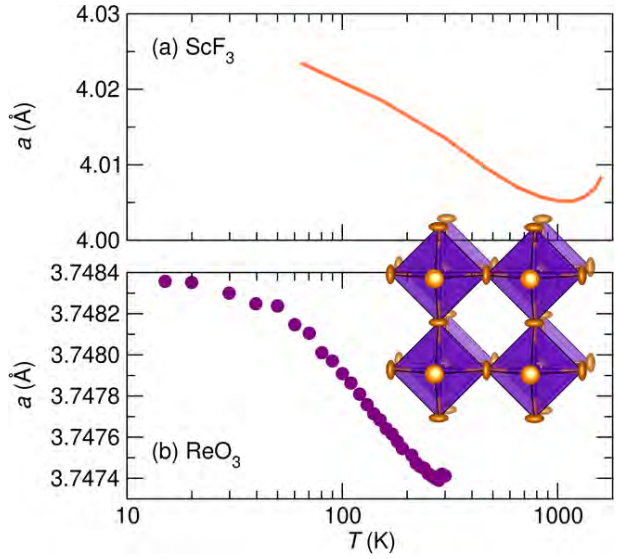

Figure 4: Lattice constant versus temperature (log scale). (a) The change in lattice constant for ScF_3; combination of synchrotron X-ray and neutron diffraction data.[85] (b) The change in lattice constant for ReO_3 based on neutron diffraction data.[27] The cubic ReO_3 structure type is shown as an overlay (95% thermal ellipsoids). Note the magnitude of the NTE is much greater for ScF_3 than for ReO_3. The Figure contains digitized data adapted with permission from Greve *et al.*[85] and Rodriguez *et al.*[27]

denced by pair distribution studies) but appears cubic on average. The source of this local symmetry breaking is thought to be the increased surface pressure from the decreased particle size. This tuning can also be achieved by Zr doping.[98] It has also been found that NTE in ScF_3 can be essentially turned off by doping with a small amount of Fe and intercalating an equal amount of Li into the vacant *A*-sites.[99] The inclusion of Li ions limits the transverse vibrations of the fluoride ions, much the same way that guest molecules can dampen NTE in other porous NTE materials.[100–104]

Redox active MF_3 materials that have been examined as intercalation materials for batteries include those where M = Ti, V, Mn, Co, and Fe.[105,106] The predominant focus has been on FeF_3 as it displays the most well behaved charge/discharge profile, a viable voltage

range (2 V – 4 V), and increased thermal stability upon lithiation.[107] However, due to the low electrical conductivity of FeF_3 (and fluorides in general), ball-milling with a conductive carbon to increase electron transport is always needed. In the case of FeF_3, a reversible capacity of 80 mAh g^1 is achievable after this process.[105] Aside from conductive carbon additives, nanostructuring the FeF_3 to increase the surface area for lithiation,[108–112] or doping with cobalt, have been studied as ways to increase conductivity. However, theory suggests that FeF_3 becomes less stable with Co-doping[113] and tends to form a tungsten-bronze related structure, a potential battery material in its own right.[114] The tungsten-bronze structure type is also observed with iron fluoride hydrate, $FeF_3 \cdot 0.33\ H_2O$, and performs similarly to the Co doped variety.[115] Lastly, there are reports that the perovskite $NaFeF_3$ can be completely (100%) desodiated/sodiated reversibly, and is of interest for future Na battery cathodes.[116]

Double fluoride ReO_3-type compounds, with the general formula *MM'*F_6, come in many varieties. Examples include the parent compound, $Sn^{2+}Sn^{4+}F_6$,[117] $M^{2+}(Zr)F_6$ compounds (where M = Fe,[118,119] Pd,[120] Co,[121] Zn,[121] Mg,[122] Cu,[123] V,[124,125] Ti,[124] Ca,[119,126] Cr[119]), $M^{2+}(Hf)F_6$ compounds (where M = V,[124] Ti,[124]), $M$$MoF_6$ compounds (where M = Na[127] and Cu[128]), $M$$NbF_6$ compounds (where M = Cr[128] and V[125,129]), and $NaSbF_6$.[130] There are examples within those compounds which display NTE,[126,131,132] gas adsorption under pressure,[126] as well as Jahn-Teller distortions governed by the M^{2+} character.[119,123,125] There are also the recent reports of the fluoride rich ReO_3-type compound, $YbZrF_7$,[133] which displays NTE below room temperature and ZTE at 300 K, and the $Mg_{1x}Zr_{1+x}F_{6+2x}$

compounds in which the degree of thermal expansion can be tuned by varying x.[134]

ReO_3-type oxyfluorides, with general formula MO_xF_y (M = Ti,[135] V,[136] Ta,[137] Nb,[135,137] Zr,[138] Mo[139]) are also known, with the first example reported in the 1950's.[137] They are predominantly tertiary compounds, but there are examples of quarternary compounds, like the non-stoichiometric $Nb_{0.55}Zr_{0.45}O_{1.1}F_{0.8}$,[138] $CrNb_2O_4F_5$ and $Fe_2Nb_3O_6F_9$,[140] and $MgNb_2O_3F_6$ and $MgTi_2OF_8$.[141] The ReO_3-type oxyfluorides have been primarily studied as intercalation materials for use in batteries,[135,136] with the greater class of oxyfluorides viewed as a favorable middle ground between oxides and fluorides, leveraging the high voltage levels of the fluorides and increased stability of the oxides (due to the more covalent M–O bonds). As is the case with all battery materials, understanding the underlying crystal chemistry of each compound is important, as anion and cation order can have a substantial impact on material performance. Recent work in this respect was on NbO_2F and $TaOF_2$, where samples prepared via solution routes (as opposed to conventional solid state methods) were reported to have vacancies and hydroxide (OH^-) ions introduced during preparation.[142] In the same study, precise solid-state preparation of the materials, and subsequent diffraction studies, facilitated the development of a supercell model to describe the anion ordering motif. Another recent example was the application of VO_2F as a cathode material,[136] which demonstrated a reversible capacity of 250 mA h g^{-1} at 2.2 V (one equivalent of Li, C/50, with graphene additive). However, if the material is cycled past 2.2 V (more than one equivalent of Li, C/50), it undergoes a conversion reaction which inhibits the cycling performance. This work was followed by a report where VO_2F was prepared via ball-

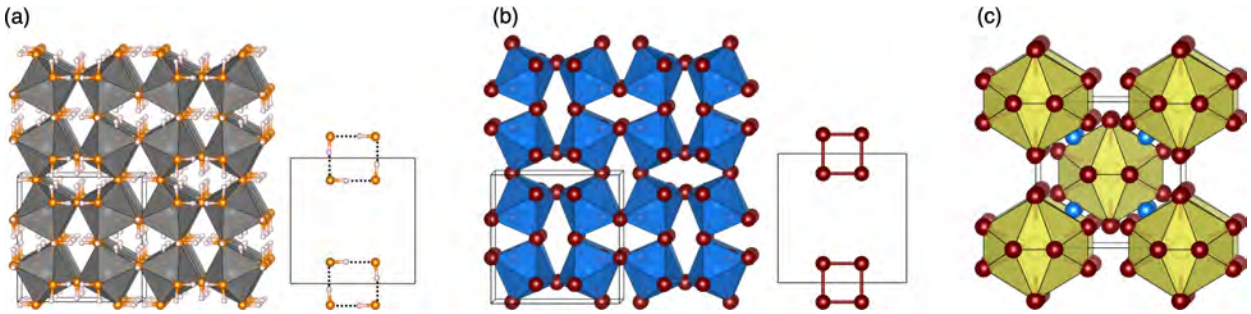

Figure 5: The highlighted structural similarity between (a) $In(OH)_3$ and (b) $CoAs_3$, drawn to scale. The bonding between As atoms follows the same motif as the "ice-rules" hydrogen bonding in $In(OH)_3$. (c) $CoAs_3$, emphasizing the 12 coordinate cavity, or cage, that can be filled with a cation. This cation "rattles" inside of the cavity, increasing thermoelectric performance via phonon scattering. Atom legend; indium = grey, oxygen = orange, hydrogen = white, cobalt = blue, arsenic = red, 12-coordinate site = yellow.

milling, as opposed to the high temperature solid-state synthesis of the original report,[143] and showed that the ball milled material had a reversable cyclability of 208 mA h g^{-1} at 2.2 V, but at an improved cycle rate of C/20. This VO_2F material also underwent an irreversible phase change if cycled to lower voltages, which has been shown by multiple groups to be a disordered rock-salt phase.[143–145] The most recent of those reports clarified the performance of the ball-milled VO_2F material,[145] and described that it delivers 276 mA h g^{-1} (1.04 mol Li) and 206 mA h g^{-1} (0.8 mol Li) at C/20 in its first and second cycles, respectively, with 97.5% capacity maintenance after 100 cycles. If taken to the irreversible rock-salt phase, 406 mA h g^{-1} (1.54 mol Li, C/60) capacity was achieved, but with only 60% capacity maintenance after 50 cycles.

Hydroxides The hydroxide perovskites [$M(OH)_3$, or $MM'(OH)_6$] are a naturally occurring class of ReO_3-type materials well known to mineralogists,[146] with some synthetic examples joining the ranks. Members of this material class are showing great promise as future

oxygen evolution reaction (OER) catalysts, but there is still much to be understood about their fundamental crystal chemistry, as the hydrogen bonding of the –OH groups governs the final structure.

The single ReO_3-type perovskite, $M(OH)_3$, includes varieties where M^{III} = Al,[147] Ga,[148] Fe,[149,150] Sc,[151] In,[151,152] Lu, [153] and Yb.[154] The Ga, In, and Fe phases occur naturally, though all except for Fe (discussed below) can be prepared synthetically. The most common preparations are metathesis reactions, usually between a MCl_3 species and NaOH (to form a gel), which is then washed and heated with more base to crystallize the compound. Early reports of the Sc,[151] In,[151,152] and Lu[153] compounds described their structures, including a neutron diffraction study to establish the locations of the hydrogen atoms.[153] In the case of $In(OH)_3$ (as shown in Figure 5 (a)), we draw attention to how the hydrogen bonding follows a four-ring (square) pattern, but there are also "zigzag" and "crankshaft" hydrogen bonding patterns, which guide the structures of the hydroxide perovskites.[146] Pure $Yb(OH)_3$ has eluded synthetic efforts, although it is known to form solid solutions (up to 25% Yb) with both $Lu(OH)_3$ and $In(OH)_3$.[154] As stated above, $Fe(OH)_3{\cdot}nH_2O$ (bernalite is its mineral name),[155] is a curious case. There are no definitive reports of a laboratory prepared ReO_3-type $Fe(OH)_3$, but there are reports of a "$Fe(OH)_3$ powder" which is distinct from the $Fe(OH)_3$ gels that form in high pH Fe^{+3} cation containing solutions. This powder, we suspect, is the amorphous version of the ReO_3-type compound, with considerable disorder due to water molecules inside the cavities. This $Fe(OH)_3$ powder has been the subject of Mössbauer and magnetic characterization in order to differentiate it from the

gels, albeit without definitive structural characterization.[149,150] For the most part, these single metal materials have fewer applications than the double hydroxides discussed below, though $In(OH)_3$ can be synthesized with nanomorphology and has been converted to the more industrially relevant In_2O_3 whilst maintaining nanostructure.[156]

There are numerous mineral examples of double perovskites, *MM'*$(OH)_6$, with a heavy predominance of stannates (the formal precursor is stannic acid, $Sn(OH)_4$). Some examples are $CaSn(OH)_6$ (burtite), $FeSn(OH)_6$ (natanite), $ZnSn(OH)_6$ (vismirnovite), and $MnSn(OH)_6$ (wickmanite). These stannate minerals crystallize in cubic space groups (except for $MnSn(OH)_6$, which is reported to be tetragonal) and exhibit cation ordering. There are also other minerals, such as $Fe^{3+}Sn^{4+}(OH)_5O$ (jeanbandyite), $NaSb^{5+}(OH)_6$ (mopungite), and $Fe^{2+}Ge^{4+}(OH)_6$ (stottite) which are not stannates. Synthetic varieties of double ReO_3 hydroxide compounds, such as $CuSn(OH)_6$,[157] CoSn(OH)6,[158] and $SrSn(OH)_6$,[159] are also known, with the latter example by Woodward and co-workers illustrating that the ionic sizes and electronegativities of the *M*-site cations are important characteristics for ReO_3-type structure formation. This was made evident by demonstrating that both $LiSb^{5+}(OH)_6$ and $BaSn(OH)_6$ both crystallize in other structural motifs.[159]

Magnetic studies of double hydroxide perovskite materials have revealed that for systems with strong charge ordering, e.g. $MnSn(OH)_6$ and $CoSn(OH)_6$, the materials are paramagnetic down to 2 K, with $MnSn(OH)_6$ displaying weak antiferromagnetic interactions at low temperature.[158] $FeSn(OH)_6$ and $FeSn(OH)_5O$ (where the former forms the

latter when left in air for a few hours) have also been examined,[160] with $FeSn(OH)_6$ exhibiting paramagnetism down to 1.4 K, and $FeSn(OH)_5O$ ordering antiferromagnetically at 4 K. Additionally, the bulk Jahn-Teller distorted $CuSn(OH)_6$[157] displays weak antiferromagnetic behaviour and a spin-Peierls transition in strong magnetic fields at about 78 K.[161]

Most interestingly though, these compounds have found recent relevance as both photo and OER catalysts. Their photocatalytic performance is linked to how, when exposed to UV light, they generate $OH^{-\bullet}$ radicals, which can degrade organic molecules.[162] The compounds $ZnSn(OH)_6$[163] and $CoSn(OH)_6$)[164] have been of particular focus. In terms of OER performance, a recent example demonstrated the power of defect engineering by showing how an argon plasma treated sample of $Co_{0.90}Fe_{0.10}Sn(OH)_6$ performed better than a nontreated sample.[165] Due to the weaker Sn–OH bonds, Ar plasma treatment selectively removes Sn to expose more active Fe and Co sites, as well as increasing the micropore size of the material. When compared to the non Ar plasma treated material, the treated sample required a much lower overpotential for catalysis (270 mV at 10 $mAcm^{-2}$, with a Tafel slope of 42.3 $mV\,dec^{-1}$). Another recent example utilized a similar SnFeNi hydroxide system,[166] but implemented an electrochemical activation process to remove the Sn^{+4} cations. When compared to the well-known OER material, IrO_2, the SnFeNi hydroxide material performed comparably. With the added benefit of being made from earth abundant metals, this is a promising field of research.

As the last examples indicated, defined control over the vacancies, and morphology,

of a double hydroxide perovskite proves essential to their use as functional materials. This kind of chemical control was previously exemplified by Nielson *et al*.[158], who demonstrated that if the hydrolysis of the Sn^{+4} ion can be kinetically controlled during the formation of $CoSn(OH)_6$ and $MnSn(OH)_6$ (by using a competing F^- anion), defined charge ordering of the metals can be promoted. This control is significant because if charge ordering can be maximized, materials like the OER catalysts should have the maximum amount of surface active sites available after Ar treatment.

Lastly, the ordering of the metals undoubtedly affects the hydrogen-bonding tendencies in certain systems, which as stated above, is a strong guide for the structure of the hydroxide perovskites. In future work, it would be worthwhile understanding how greater synthetic control can encourage certain hydrogen bonding arrangements (different polymorphs). Mineralogists have highlighted some of the significant, more fundamental, questions in this class of materials,[146] with the overarching problem being that the correct structures (e.g. space groups) of most hydroxide perovskites are not definitive. This is an area where better synthetic control can elucidate why certain polymorphs (tilts caused by hydrogen bonds) are favored in certain systems, with variable temperature and pressure[167] studies unraveling the poorly-understood phase transitions of the materials. Finally, with an average cavity diameter of 4.5 Å, many small molecules could be intercalated, but understanding how the hydroxide groups may play a role in guest-molecule intercalation is an open question.

Alloys with the ReO_3-type structure Skutterudite is a mineral that was named after the city of Skotterud, Norway, where it was first discovered in 1845. The naturally occurring version is a cobalt arsenide, $CoAs_3$, which also contains some nickel and iron on the cobalt site (Figure 5 (b)). The structure of the mineral form was first examined by X-ray diffraction in 1928 by Oftedahl,[168] who showed that it was cubic with space group $Im\bar{3}$, and a more precise determination was carried out by Mandel and Donohue in 1971.[169] The structure is formed from a network of corner-sharing $CoAs_6$ octahedra, as in ReO_3, but these are sufficiently tilted that the arsenic atoms form approximately planar As_4 units (Figure 5). In order for the As_4 unit to be square, the *x* and *y* values of the As coordinates must obey the so-called Oftedal relationship, $2(y + z) = 1$, but in the determination by Mandel and Donohue the values of *x* and *y* are such that the As_4 unit is rectangular with edges of 2.57 and 2.46 Å, respectively. There is clearly a significant amount of As–As bonding in $CoAs_3$, so the system can be regarded as a Zintl phase.[170] The structure is very similar to that of $In(OH)_3$, where the hydrogen bonding creates a square pattern (Figure 5), and indeed the two systems adopt the same $Im\bar{3}$ space group. Several closely-related families of naturally-occurring and synthetic alloys adopt the skutterudite structure, and this MX_3 family is known for *M* = Fe, Co, Ni, Ru, Rh, Ir, Os and *X* = As, Sb, P. However, we are not aware of any examples with *M*-site ordering, which is common for more ionic systems, as discussed previously.

The so-called "filled skutterudites" represent an exceptionally important extension of this family. The first examples were reported by Jeitschko[171] and can be thought of as *A*-

site deficient perovskites, A_xMX_3, with $x = 0.25$ (i.e. their general composition is AM_4X_{12}). We have chosen to include them in this review because they are closer in composition to ReO_3 than perovskite and they have a wide range of very interesting electronic properties. Typical cases include systems such as LnM_4X_{12}, where Ln = rare-earth, M = Fe, Ru, Os, and X = P, As, Sb. Superconductivity below 4.08 K and 7.20 K was reported for $LaFe_4P_{12}$ and $LaRu_4P_{12}$, respectively, in 1981 by G. P. Meisner[172] and magnetic ordering was found to occur at even lower temperatures when La is substituted by magnetic rare-earth elements such as Ce, Pr and Nd (superconductivity was not observed in the magnetic systems).

The initial discovery of superconductivity in $LaFe_4P_{12}$ and $LaRu_4P_{12}$ attracted the attention of the condensed matter physics community and lead to a large body of work on these materials in subsequent years. Beyond the studies on superconductivity, the most exciting development was the establishment by Sales *et al*. in 1996 that some of the filled skutterudites were excellent thermoelectric (TE) materials with, at that time, figures of merit, ZT, in excess of 1.0.[173] It was already recognized that conventional skutterudites had the potential to be good thermoelectrics,[174] and the filled skutterudites offer the opportunity for further enhancement. In particular, the rattling of the cations in the large A-site voids (Figure 5 (c)), along with the ease with which disorder can be introduced into these systems, both contribute to their excellent performance. These factors reduce the lattice thermal conductivity by scattering phonons and contribute to excellent TE performance, as discussed by Snyder and Toberer.[175] Subsequent developments in this area, including the use of filler cations with different charges, enabled the tuning of the carrier

density, leading to systems with TE performance that approach many of the better performing materials.[176] For example, $CoSb_3$ filled with various combinations of Ba, La and Yb have *ZT* values of up to 1.7 at 850 K, e.g. for $Ba_{0.08}La_{0.05}Yb_{0.04}Co_4Sb_{12}$.[177]

While the bulk of the work on skutterudites for thermoelectric and other applications has focused on the filled systems, as described above, there has been a recent report of an excellent figure of merit for an unfilled system in which the thermal conductivity was minimized by controlling the nanostructure and microstructure of the material by means of careful annealing.[178] In this way, a *ZT* of 1.6 was reported for a synthetic alloy of composition $Co_{23.4}Sb_{69.1}Si_{1.5}Te_{6.0}$, despite the absence of rattling cations in the *A*-site cavity. When the nano/microstructure was not controlled by annealing, the thermal conductivity was approximately 4-5 times higher, leading to a 60% decrease in *ZT*.

Cyanides and other Prussian blue analogue materials In view of the extensive and historical literature on perovskite-related cyanides such as Prussian Blue, $Fe_4[Fe(CN)_6]_3{\cdot}xH_2O$,[179] it is not surprising that similar ReO_3-type cyanides are known. These materials are generally referred to as Prussian blue analogues (PBAs), though the literature does not differentiate between those that have cations on the *A*-sites (i.e. they are perovskites) and those that do not (i.e. they are ReO_3-types). Several cyanide based examples with the ReO_3-type structure, however, are known, including a number of bimetallic systems such as $M^{II}Pt^{IV}(CN)_6$,[180] $Ga^{III}Fe^{III}(CN)_6$,[181] and $Fe_4[Ru(CN)_6]_3{\cdot}18H_2O$.[182] The cavities are larger than those of the simple oxides and fluorides, so there is often solvent, typically water,

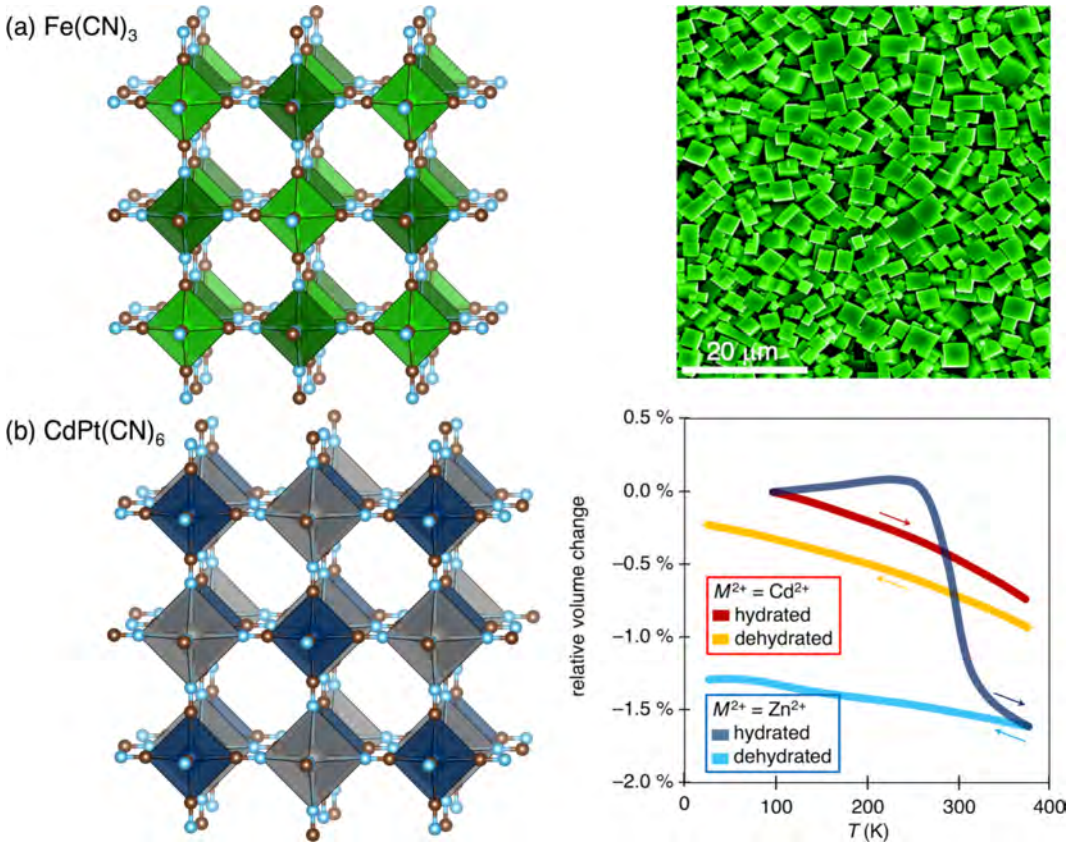

Figure 6: (a) Structure of $Fe(CN)_3$, with colorized SEM image of Berlin Green microcubes (SEM figure adapted with permission from Yang et al.[183] (b) The structure of dehydrated $Cd^{II}Pt^{IV}(CN)_6$ is drawn alongside a graph showing relative volume change as temperature is varied for $M^{II}Pt^{IV}(CN)_6$ (M = Zn, Cd). Intercalated water within the two compounds changes their NTE behavior by dampening the transverse vibrations of the –CN ligands. Data adapted with permissiom from from Goodwin *et al.*[100] Atom legend; Iron = light/dark green, carbon = brown, nitrogen = light blue, cadmium = grey, platinum = navy.

found within them. Anhydrous materials, solvated systems, and thiocyanates will be the focus of this section.

The simplest example is probably $Fe[Fe(CN)_6]$, i.e. $Fe(CN)_3$, which crystallizes in a doubled ReO_3-type structure with alternate Fe^{III} ions coordinated by six carbons and six nitrogens, respectively, from the cyanide ions. It is sometimes known as Berlin Green be-

cause of its historical use as a pigment in paintings (Figure 6a).[183] The cation ordering, which gives rise to the doubling of the basic ReO_3 unit cell, is made possible by having the two iron sites in low-spin d^5 (FeC_6) and high-spin d^5 (FeN_6) states, respectively, as discussed below. The cavity in the as-synthesized material contains some water, but this can be removed under vacuum and samples of the anhydrous material have been studied as a function of temperature by synchrotron X-ray diffraction. Like many ReO_3-type structures, it exhibits pronounced NTE over a wide temperature range, in this instance from 100 K to 450 K.[179] As in the ReO_3-type oxides and fluorides, the NTE is associated with transverse vibrations of the carbon and nitrogen atoms of the cynaides; these are especially strong for the nitrogen atoms due to the longer Fe–N bonds. In an interesting variation on the above theme, a guest dependence of the NTE was reported for $M^{II}Pt^{IV}(CN)_6$ (M = Zn, Cd) by Goodwin *et al.*,[100] which showed that by including an intercalant species the transverse vibrations are dampened and NTE is suppressed (Figure 6b). As a point of interest, this dampening of NTE via intercalation is also observed for a related (non-ReO_3-type) porous rare earth cyanide compound,[184] and illustrates the similar structure-property relationship between the systems.

The magnetic properties of a hydrated form of $Fe[Fe(CN)_6]$ have been studied by low temperature neutron diffraction, Mössbauer spectroscopy and magnetic susceptibility methods, and the system is found to undergo a paramagnetic to ferromagnetic phase transition on cooling to 17.4 K.[185] This is consistent with the weak ferromagnetic exchange coupling that is expected between low-spin d^5 Fe^{III} and high-spin d^5 Fe^{III} via the cyanide

linker. There is also a long history of bimetallic PBAs that have been studied for their magnetic properties,[186] mainly in the context of molecular magnetism. This is a particularly fruitful area because the alternation of two different octahedrally coordinated cations that are linked by cyanide groups can give rise to a wide range of antiferromagnetic, ferromagnetic, and ferrimagnetic behavior. Most of the work in this area, however, has focused on systems with cations on the *A*-sites, so they are beyond the scope of this work, but there are a few examples of materials that adopt the ReO_3-type structure. The most striking case is probably a phase with the approximate composition $VCr(CN)_6{\cdot}xH_2O$, which has a ferrimagnetic ordering temperature of 315 K due to strong superexchange interactions between the vanadium and chromium (III) ions.[187] The system is more complex than it initially appears, however, because vanadium is present in both the V^{II} and V^{III} oxidation states, leading to a variety of possible magnetic interactions. Another example are the cobalt(II)-manganese(II)-chromium(III) compounds ($Co_xMn_{1-x}[Cr(CN)_6]_{2/3}{\cdot}zH_2O$,[188] which depending on the compound of choice within the family, can be tuned between ferromagnetic and antiferromagnetic coupling depending on relatively humidity. The humidity-induced variations in the compounds are related to the coordination geometry of the Co ions, which in certain variants are undercoordinated due to $[Cr(CN)_6]$ vacancies, and can be coordinated to by water. Conversely, a counter example would be the iron-ruthenium PBA, ($Fe_4[Ru(CN)_6]_3{\cdot}18H_2O$),[182] which was examined in part for its potential magnetic behavior but found to display no ordering above 1.8 K. This material, however, is interesting as it demonstrates the effect of electron localization when compared to its

Prussian Blue parent and potassium intercalated sibling ($K_{1.2}Ru_{3.6}[Ru(CN)_6]_3$), as the iron-ruthenium compound has decreased electrical conductivity and blue shifted optical intervalence charge transfer (IVCT) transitions.

Many PBA materials have also been explored for their potential applications in sodium ion batteries,[189] but work in this area has been hampered by low capacity utilization and poor cyclability. In the case of $Fe[Fe(CN)_6]$, the use of nanoparticles overcame these drawbacks, giving rise to a device with good kinetics, capacity and lifetime[190,191] (we note that this strategy also worked for FeF_3, as discussed earlier). There has also been work on both lithium[192] and potassium[193] batteries with $Fe[Fe(CN)_6]$.

Finally, we would like to mention a very recent report of the first examples of thiocyanates with the ReO_3 structure.[194] The thiocyanate systems have the general composition $M^{III}[Bi(SCN)_6]$ with M = Fe, Cr, Sc, and there is strict alternation of the Bi^{III} with the trivalent transition metal ions. This ordering is not too surprising, given the expected local bonding preference between sulfur and Bi^{III}. All the materials have band gaps in the visible or infrared regions, with the iron compound being as low as 1.20 eV, so they are strongly coloured and might be useful for applications that involve light harvesting. The *A*-site cavity would be expected to be even larger than those in the cyanides described above, but in fact the porosity is reduced by substantial monoclinic distortions of the hypothetical cubic structures. Nevertheless, the Cr^{III} compound exhibits reversible adsorption and desorption of water, forming a monohydrate. As in some of the other cyanides, the guest molecules

have an impact on the thermal expansion, but there is no evidence of NTE in these systems.

Borohydrides M^{III} borohydrides, $M(BH_4)_3$, sometimes crystallize in the ReO_3 topology depending on synthetic route and the size of the metal ion. One well studied example is $Y(BH_4)_3$ (Figure 7) (a), a potential hydrogen storage material, which is attractive because it degrades to H_2 gas and solid YB_4 under 1–5 bar of partial hydrogen pressure (i.e. a typical operating condition of a H_2 storage system).[195,198,199] Unlike other M^{III} borohydrides which have common by-products like elemental boron or diborane, YB_4 is more easily coverted back to $Y(BH_4)_3$, enabing a charge/discharge cycle.[200] Crystallographically, $Y(BH)_4$ is reminiscent of the oxide ReO_3-type phases as it has two ReO_3-type polymorphs, α and β, which are both generated on synthesis by ball-milling and coexist at room temperature. However, the more dense and distorted α-$Y(BH_4)_3$ phase can be converted to the less dense and cubic β-$Y(BH_4)_3$ phase upon heating to 160°C - 180°C, ultimately decomposing past 190°C. Unlike the oxides, though, both phases show monotonic positive thermal expansion.

A more systematic study of the M^{III}–BH_4 reaction system with M = lanthanides[201] demonstrated the importance of the ionic radius of the M metal in determining whether the ReO_3-type structure type formed. Using ball-milling with a $LiBH_4$ precursor, the larger lanthanides (La, Ce, Pr, and Nd) formed only the cubic $LiM(BH_4)_3Cl$ structure, while those closer in size to Y (Sm, Gd, Tb, Dy, Er, and Yb) all formed the α-$Y(BH_4)_3$ structure. The elements Sm, Er, and Yb are also stable in the β-$Y(BH_4)_3$ structure, under certain condi-

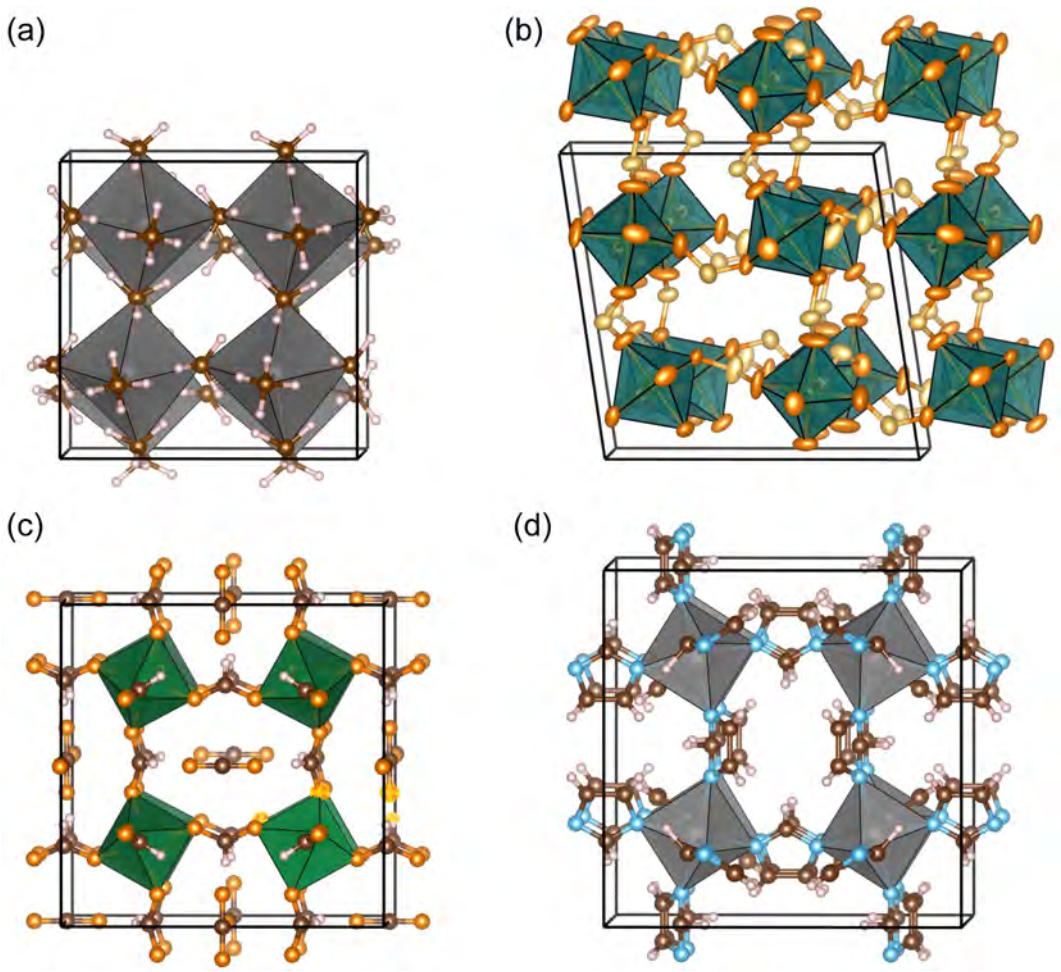

Figure 7: (a) Crystal structure of α-Y$(BH_4)_3$. Bonds are drawn between the Y and B atoms, to emphasize the ReO_3- type structure, though they are not present. It is in fact the bonding between Y and H atoms that guides the structure to be ReO_3-type.[195] Atom legend; yttrium = grey, boron = brown, hydrogen = beige. (b) Representative crystal structure with the ReO_3 topology of α-$M(H_2PO_2)_3$, shown for M = Ga in the $P2_1/n$ space group (90 % ellipsoids, H removed for clarity).[196] Atom legend; gallium = turquoise, oxygen = red, phosphorous = orange, hydrogen = beige. (c) $Fe(HCOO)_3$ with interstitial CO_2 (water removed for clarity).[197] Atom legend; iron = green, oxygen = orange, carbon = brown, hydrogen = beige. (d) $In(im)_3$. The imidazolate anions arrange in an alternating pattern in $In(im)_3$ to accommodate their size. Atom legend; indium = grey, nitrogen = blue, carbon = brown, hydrogen = beige.

tions. Further experimentation yielded the distorted ReO_3-type $M(BH_4)_3$ (M = La, Ce) through the reaction of MCl_3 and $LiBH_4$ in toluene at room temperature, followed by extraction of $M(BH_4)_3$ using dimethyl sufide [$S(CH_3)_2$] to form a solvated phase. Subsequent loss of $S(CH_3)_2$ from the adduct yields the $M(BH_4)_3$ phase.[202] The $S(CH_3)_2$ templating strategy combined with halide-free reagents (rare earth hydride and $S(CH_3)_2{\cdot}BH_3$) was then applied generally to generate new structures, include the cubic $Pa\bar{3}$ α-$Pr(BH_4)_3$ and α-$Nd(BH_4)_3$ structures,[203] and α-$Ce(BH_4)_3$, β_2-$Pr(BH_4)_3$, α-$Lu(BH_4)_3$, β-$Pr(BH_4)_3$.[204] The latter paper also identified the structures of the $S(CH_3)_2$-adduct intermediates as layered phases, reminiscent of layered perovskites. Although the ReO_3 phases are not direct precursors, the related $Li(M(BH_4)_3)Cl$ phases have potential application as fast Li-ion conductors for solid-state battery electrolytes and gas storage,[205] with some lithium borohydride phases having been tested in devices.[206]

Hypophosphites Until recently, the compound $V(H_2PO_2)_3$ was the only example of a hypophosphite containing ReO_3-type compound,[207] but following work by the authors here, it is now understood to be a member of a polymorphic family of ReO_3-type materials, $M(H_2PO_2)_3$, where M = Al, Ga, and V [Figure 7 (b)][196] There are four polymorphs seen in this family, (α, β, γ, δ), with each polymorph displaying different degrees of tilts and shifts of the M octahedra. Furthermore, each polymorph is preferred to varying degrees depending on the M, with each $M(H_2PO_2)_3$ forming at least two of the four polymorphs. The high pressure (above 1 GPa) δ phase has been observed for $Ga(H_2PO_2)_3$, which normally prefers the less dense α phase at STP. Synthetic control between each preferred polymorph is still

an open question, but to obtain at least one pure polymorph in each metal system, using an acid soluble oxide precursor is prefered (such as γ-Al_2O_3 instead of corundum for the Al system). Interestingly, the compound $Al(H_2PO_2)_3$, though its structure was unreported, is known to be an excellent bromine-free flame retardant in polymer blends.[208] As the structure was only just reported, there are potentially advantages to using one polymorph as opposed to another if synthetic control can be leveraged.

3 Metal-Organic Frameworks

Systems with Organic Linkers We have seen in the previous section that there are several inorganic systems with the ReO_3-type structure in which the anionic linkers are polyatomic. Such compounds present an interesting variation on the perovskite topology because the vacant *A*-site may create a space that is large enough to accommodate adsorbed solvent or small gas molecules. This is seen in the cyanides and the thiocyanates, though the cavity in the hypophosphites appears to be too small for even monatomic neon.[196] Since the cavities defined by the larger molecular *X* sites may even be large enough to deliver permanent porosity, there is a significant similarity between such systems and metal-organic frameworks (MOFs). It is not surprising, therefore, to find that there are several examples of ReO_3-type materials in which the linker is an organic anion, and such materials can be properly regarded as MOFs. Examples of such systems, which are discussed below, include materials based on a wide variety of organic linkers, e.g. formates, azolates, guanidinates, and other, more complex ligands.

Formates, $M^{III}(HCOO)_3$ M = Al, V, Fe, Ga, In ABX_3 perovskite-type phases where X = $(HCOO)^-$, formate, have been extensively studied as they are easily prepared using solution synthesis and show a wide range of interesting ferroelectric, magnetic, and multiferroic properties.[209–211] The classical Goldschmidt tolerance factor equation,[212] which predicts the relative radii of cations and anions that are compatible with simple inorganic perovskite formation, has been extended to hybrid perovskites[213,214] and can be used to predict the sizes of the A cations that will stabilize the perovskite structure in systems such as $AM^{II}(HCOO)_3$. Because the cavity is quite large, it is not surprising that quite large protonated amines, such as dimethylammonium, $(CH_3)_2NH_2^+$, are required. As an extension of this observation, it is also not surprising to find that ReO_3-type systems of composition $M^{III}(HCOO)_3$ have been reported, but only in the presence of neutral guest molecules that occupy the A site cavities.

A 1965 publication provided evidence that $V(HCOO)_3{\cdot}HCOOH$ may crystallize in the ReO_3 topology,[215] but a full structure determination for this compound has not been performed to date. However, the powder diffraction pattern[215] was indexed on a body-centred cubic structure that is consistent with M(III) formates reported more recently,[197] and other measures such as density are also close to the values reported for the Fe phase (V^{3+} and Fe^{3+} having similar molecular weights and radii). The neutral formic acid molecule, HCOOH, would be expected to occupy the A site.

The most recent work[197] on the $M^{III}(CHOO)_3$ systems (M = Al, Fe, Ga, In) confirmed

that these phases, which can be readily formed by solvothermal or reflux methods, adopt an ReO_3-type structure with neutral *A*-site occupants assigned as combinations of H_2O, CO_2, and HCOOH [Figure 7 (c)]. All of these phases crystallize in the cubic $Im\bar{3}$ space group with a = 11.4 Å– 12.2 Å. Unlike many of the other carboxylate MOFs, the molecules occupying the *A*-sites in the $M^{III}(CHOO)_3$ systems could not be liberated while keeping the framework intact, suggesting that these molecules may have a structural role through strong hydrogen bonding or that the *M*–O bonds are insufficiently strong to stabilize the framework in the absence of guests. An alternate form of the $Fe(CHOO)_3$·guest ReO_3-type phase was also reported,[216] crystallizing in the trigonal $R\bar{3}c$ space group with a = 8.2 Å, c = 22.6 Å. It exhibits antiferromagnetic ordering at low temperatures.

The formate ReO_3-type compounds could perhaps be regarded as the simplest MOF systems and can be made from inexpensive, earth-abundant starting materials. What is particularly interesting is that they show a very strong preference for forming in the presence of CO_2, and $Al(HCOO)_3{\cdot}x CO_2/y H_2O$ can be obtained by bubbling CO_2 through an aqueous solution containing $Al(OH)_3$ and formic acid.[197] The fully stoichiometric phase, $Al(HCOO)_3{\cdot}CO_2$, has yet to be achieved, but with a potential CO_2 loading of greater than 21 wt%, it is an interesting option for CO_2 storage.

Nitrogen-containing Organic Linkers In light of what has been reported for the formates, where the ReO_3-type MOFs contain metal-oxygen bonds, it would be reasonable to expect that MOFs with the ReO_3-type structure might also form with nitrogen-containing

organic linkers that are capable of metal-nitrogen bonding. This has so far been realized for guanidinates, 1,2,4-triazolates, and imidazolates, though there are clearly other potential systems that might be feasible.

Only one guanidinate with the ReO_3-type structure is known to exist, $Yb[C(NH_2)_3)_3$.[217] This phase was synthesized in liquid ammonia and crystallizes in the cubic $Pn\bar{3}$ space group with a = 13.5 Å. Braced by the extensive hydrogen bonding between guanidinate anions, it has a relatively low density (1.9 g cm^{-3}) and potential voids in the structure. Unlike many of the simple inorganic ReO_3-type systems, $Yb(CN_3H_4)_3$ shows positive thermal expansion rather than NTE. It is interesting to note that guanidine derivatives can play a role in perovskite-related materials both as an anionic linker (as in the present Yb phase) and as an *A*-site cation (as in the formate perovskites[218]). Clearly the control of pH is very important in determining which of these roles it is able to play.

While azolates represent a well-known building block for MOFs (particularly ZIFs, where imidazolates are used as linkers), they are primarily used in tetrahedral coordination with *M*(II) cations. Nevertheless, there are a small number of ReO_3-type structures based azolates. $Yb(tz)_3$ (tz = 1,2,4-triazolate) was prepared from Yb metal and a melt of the azole, crystallizing in the cubic $Pm\bar{3}m$ space group with a = 6.8 Å.[219] $Yb(tz)_3$ is arguably not strictly an ReO_3-type as half of the tz ligands coordinate η_1 while the other half coordinate η_2, giving ytterbium a coordination number of nine; however, the overall topology is ReO_3-like. This phase is well-packed and shows no potential porosity. $Ga(trz)_3$

(trz = 1,2,4-triazolate) was later reported by the same group,[220] forming at the interface between the immiscible liquid metal and liquid triazole. This phase crystallizes in the cubic $I23$ space group with a = 12.3 Å, and gas sorption testing showed that Ga(tz)$_3$ is also a dense framework with no accessible porosity. We are not aware of any ReO_3-type structure based on 1,2,3-triazolate linkers.

Most recently, imidazole (im) was successfully used to form In(im)$_3$·*x*G (*G* = guest) ReO_3-type phases via multiple pathways including ionothermal, solvothermal, and solventless syntheses.[221] Three phases were obtained - I, II, and III - with structural parameters of $Im\bar{3}$, a = 13.0 Å; $R\bar{3}$, a = 18.9 Å, c = 10.5 Å; and $R\bar{3}$, a = 9.1 Å, c = 22.3 Å, respectively [Figure 7 (d)]. While gas sorption showed no accessible porosity, varying amounts of unbound neutral molecules appeared to be trapped inside the framework cavities of phases I and II. Phase III was reported as a completely dense, guest-free structure. All structures were solved from PXRD, and the identities and quantities of neutral guest molecules in I and II were assigned by NMR to a range of molecules including solvent and solvent decomposition products.[221] The structures were distinguished by different octahedral tilting patterns. Phases I and II showed a reversible, discontinuous, hysteretic phase transition at ca. 90°C. The synthesis method affected the transition temperature, and it was suggested that this was due to the different guest molecules trapped within the framework. It would seem unlikely that In^{III} is the only trivalent cation capable of forming ReO_3-type networks with imidazolate, so this seems to be a very interesting area for future exploration.

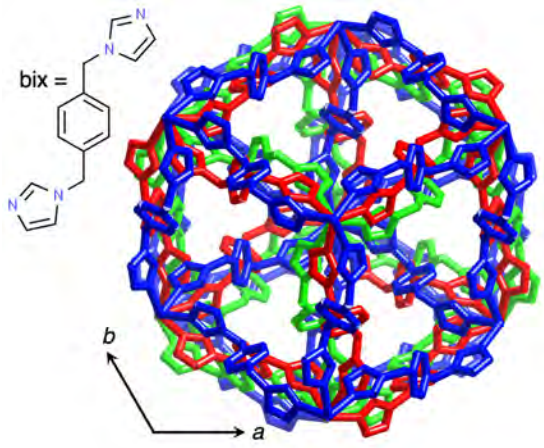

Figure 8: Triply interpenetrating MOF based on a *bis*-imidazole ligand. Figure was adapted with permision from Abrahams *et al.*.[222]

Systems with More Complex Linkers and Interpenetration There are several examples of positively charged ReO_3-type MOF frameworks with large organic linkers and charge-compensating anions in the *A*-site cavities,[223] but these are more like perovkites than ReO_3 systems (albeit with inverse polarity). They are sometimes referred to in the MOF literature as having the α-polonium structure type (α-Po being the only simple cubic metal structure), irrespective of the framework being charged and the presence of anions in the *A*-site cavities. An important example is provided by the large, neutral *bis*-imidazole ligands (Figure 8), which forms ReO_3-type frameworks with Cd^{2+} nodes.[222] What is particularly interesting is that the frameworks are triply interpenetrating, presumably to reduce the unoccupied space in the channels. Such behaviour is also seen in some of the MOF-5 related materials discussed below. The positive charges of the frameworks in these structures are balanced by nitrate or tetrafluoroborate anions which sit in the small cavities created by the interpenetrating ReO_3 nets. One would imagine that neutral frameworks of

this type could be obtained by using a trivalent cation in combination with anionic ligands.

MOFs with Polyatomic *B*-site Cations In this final section on MOFs with the ReO_3-type structure, we shall focus on an even more complex group of materials in which the cations on the *B*-site are polyatomic clusters, again linked by organic ligands. The most iconic example is MOF-5, shown in Figure 9, where tetrahedral $Zn_4O_6^+$ clusters are connected by 1,4-benzenedicarboxylate (1,4-bdc) anions to form a 3-D network of composition $[Zn_4O](1,4\text{-bdc})_3$ [Figure 9 (a)].[17] This important discovery from Yaghi's group lead to another concept known as reticular synthesis,[224,225] whereby structures with even larger cavities could be obtained by using longer linkers, as shown in Figure 9 (b). By so doing, it is possible to tune the porosity of the MOF system for specific applications. This family of MOFs is, therefore, justifiably famous for being a model for the optimization of porous frameworks for applications in separation and catalytic processes.[226] We note that interpenetration is often found in structures based on the longer linkers used to synthesize some of the IRMOF materials, though steps can be taken to mitigate this outcome.

There can be endless variations on the MOF-5 theme if we allow for the possibility that the 1,4-bdc linker might bear substituents on the benzene rings. Typical examples include $–NH_2$, –Br, –Cl, $–NO_2$.[228] Yaghi refers to such systems as multivariate MOFs on account of the range of compositional variations that are possible, such as combining eight distinct functionalities into a single phase. The chemical variations are not of solely academic interest, since it is possible to tune the adsorption behaviour of the MOF for partic-

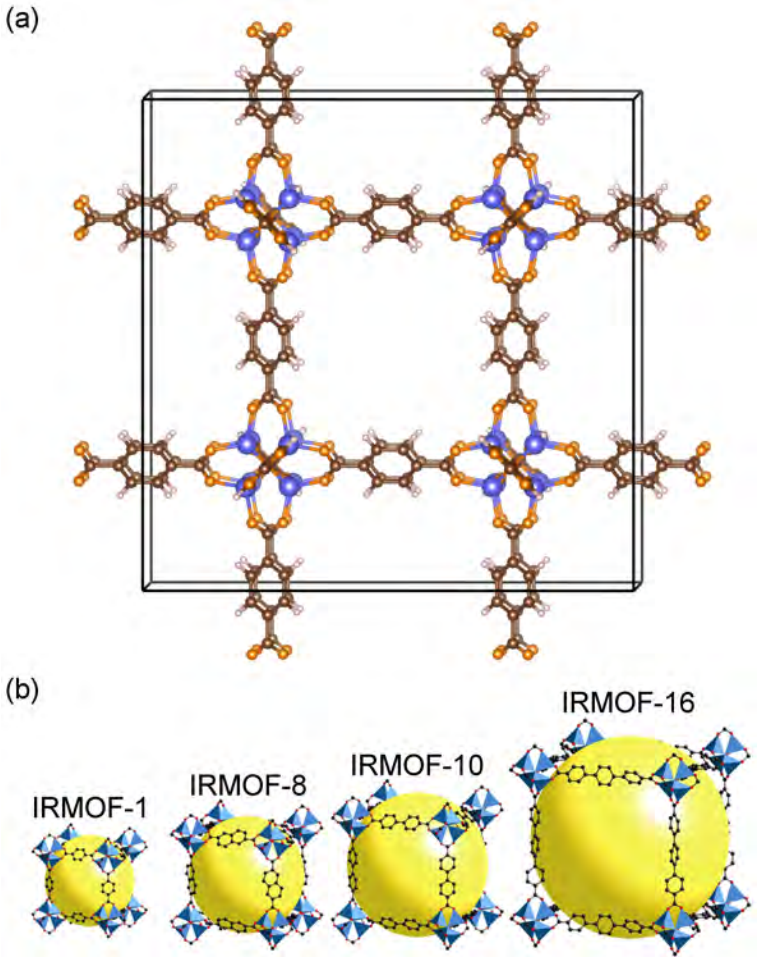

Figure 9: (a) The structure of the metal-organic framework, MOF-5, with a Zn_4O unit on the *M*-site, 1,4-bezenedicarboxylate anions on the *X*-site, of an ReO_3 topology.[17] This structure type is referred to as pcu (primitive cubic) in the MOF community. Atom legend; zinc = light blue, oxygen = orange, carbon = brown, hydrogen = white. (b) Isoreticular series of MOFs, where IRMOF-1 = MOF-5. Panel b was from Rosi *et al.*[227]

ular applications. In one instance, the selectivity for CO_2 adsorption compared with CO could be enhanced by 400% by fine-tuning the composition.[228]

There are symmetry constraints on the types of systems that can form an ReO_3-type network, since the building unit at the *B*-site node must be compatible with 6-fold connectivity, as discussed in a review by Zaworotko *et al*.[229] This is achieved in MOF-5 by using the two oxygens from one end of the 1,4-bdc carboxylate linker to bond to two different zinc ions in the cluster. In spite of this constraint, there are many other examples of systems that adopt the ReO_3-type structure (which is often referred to as the pcu - primitive cubic - topology in the recent MOF literature, though this appellation is sometimes interpreted more loosely than we have done in this review). Eye-catching examples include a system in which the nodes use $Cu_2(CO_2)_4$ paddlewheel clusters as vertices.[230]. To give a sense of the potential scope of this area, we note that Snurr and Hupp explored the methane storage and delivery capacity of 122,835 hypothetical pcu frameworks[231] from the MOF database of Wilmer *et al.*,[232] though the vast majority of these have never been synthesized.

There are many other MOFs in the literature that are described as PCU-type that we have not included here because they do not preserve the cubic or pseudo-cubic architecture of the ReO_3-type structures. Typically they have different linkages along different axes, such as the pillared-layered examples[233,234] and other structures based on paddlewheel nodes.[235]

4 Concluding Remarks

The chemical diversity of materials with the ReO_3-type structure is much greater than we had imagined when we began to think about this article in the summer of 2018. Furthermore, their properties and applications, both actual and potential, have also surpassed our expectations. The timeline shown in Figure 2 highlights some of the important systems that have been developed over the last eighty-plus years, from their initial discovery or structural characterization to the demonstration of their most striking properties. In addition to the remarkable range of their behaviour, we are struck by the long gaps between the initial discoveries of several of the materials and the establishment of their functionalities. In the case of ScF_3, for example, seventy years elapsed between the first structural characterization in 1939[236] and the recognition of its outstanding NTE behaviour in 2010! At the same time, several new ReO_3-type families of been reported in the last decade, including the borohydrides, hypophosphites, guanidinates and imidazolates, though the properties of these new families have yet to be explored.

One of the most exciting discoveries in the very recent past concerns a 2015 report that hydrogen sulfide, H_2S, transforms to H_3S under high pressure and that this new phase is superconducting with a Tc of 203 K.[237] This possibility was predicted in 2014[238] and subsequent work in 2016 has indicated that the superconducting H_3S phase adopts a doubly interpenetrated ReO_3 structure.[239] However, others have claimed that the superconducting phase is $(SH^-)(SH^{3+})$ and adopts the perovskite structure with (SH^-) on the *A*-site,[240] and

Table 1: Compilation of cases where the ReO_3 analogue of a known perovskite family is unknown, or *vice versa*. The unknown phases are labled with "NR" (not reported). In some cases, e.g. with 1,2,3-triazole, both are unknown but might be expected to form.

Perovskite family	ReO_3 analogue
(AmineH)PbX_3	BiX_3 (NR)
$A^{I}B^{II}(OH)_3$ (NR)	$M^{III}(OH)_3$
(AmineH)$M^{II}(N_3)_3$	$M^{III}(N_3)_3$ (NR)
(AmineH)M^{II}(Gua)$_3$ (NR)	M^{III}(Gua)$_3$
(AmineH)M^{II}(Im)$_3$ (NR)	M^{III}(Im)$_3$
(AmineH)M^{II}(1,2,4-triazole)$_3$ (NR)	M^{III}(1,2,4-triazole)$_3$
(AmineH)M^{II}(1,2,3-triazole)$_3$ (NR)	M^{III}(1,2,3-triazole)$_3$ (NR)
(AmineH)M^{II}(tetrazole)$_3$ (NR)	M^{III}(tetrazole)$_3$ (NR)

recent calculations broadly support the idea of such a disproportionation of H_2S.[241]

We noted at the beginning of the article that most of the ABX_3 perovskite families can form ReO_3 analogues, and *vice versa*, so it is appropriate at this point to revisit this issue and identify the systems where this has not been established. Table 4 shows a number of cases where the analogues are not known, or even where neither form is known but could potentially exist. In some cases, such as the ReO_3 form of BiI_3, the compound prefers a layered structure, which is presumably stabilized by strong van der Waals interactions between the iodide ions. In the case of the hypothetical $A^{I}B^{II}(OH)_3$, it might be that the protons that protrude into the *A*-site cavity render it unsuitable for hosting a metallic cation. However, there are several nitrogen-containing linkers that might lend themselves to the formation of new ReO_3-type or perovskite families, though we note that some of these may be high energy materials, such as the azides and the tetrazoles. Future work in these areas is certainly needed and has the potential to produce new phases with interesting and unusual properties.

Conflicts of interest

There are no conflicts to declare.

Acknowledgments

HAE thanks the National Research Council for financial support through the Research Associate Program (RAP). AKC thanks the Ras al Khaimah Centre for Advanced Materials for financial support.

Competing Interests The authors declare that they have no competing financial interests.

Bibliography

1. Kojima, A., Teshima, K., Shirai, Y. & Miyasaka, T. Organometal halide perovskites as visible-light sensitizers for photovoltaic cells. *J. Am. Chem. Soc.* **131**, 6050–6051 (2009).

2. von Hippel, A. Ferroelectricity, domain structure, and phase transitions of barium titanate. *Rev. Mod. Phys.* **22**, 221–237 (1950).

3. Callaghan, A., Moeller, C. W. & Ward, R. Magnetic interactions in ternary ruthenium oxides. *Inorg. Chem.* **5**, 1572–1576 (1966).

4. Wu, M. K. *et al.* Superconductivity at 93 K in a new mixed-phase Y-Ba-Cu-O compound system at ambient pressure. *Phys. Rev. Lett.* **58**, 908–910 (1987).

5. von Helmolt, R., Wecker, J., Holzapfel, B., Schultz, L. & Samwer, K. Giant negative magnetoresistance in perovskitelike $La_{2/3}Ba_{1/3}MnO_x$ ferromagnetic films. *Phys. Rev. Lett.* **71**, 2331–2333 (1993).

6. Moreira dos Santos, A. *et al.* Evidence for the likely occurrence of magnetoferroelectricity in the simple perovskite, $BiMnO_3$. *Solid State Commun.* **122**, 49–52 (2002).

7. Cheetham, A. K. *et al.* Multiferroic behavior associated with an order-disorder hydrogen bonding transition in metal-organic frameworks (MOFs) with the perovskite ABX_3 architecture . *J. Am. Chem. Soc.* **131**, 13625–13627 (2009).

8. Ye, H.-Y. *et al.* Metal-free three-dimensional perovskite ferroelectrics. *Science (New York, N.Y.)* **361**, 151–155 (2018).

9. Momma, K. & Izumi, F. VESTA 3 for three-dimensional visualization of crystal, volumetric and morphology data. *J. Appl. Cryst.* **44**, 1272–1276 (2011).

10. Li, W. *et al.* Chemically diverse and multifunctional hybrid organic-inorganic perovskites. *Nat. Rev. Mater.* **2**, 16099 (2017).

11. Woodward, P. M. Octahedral tilting in perovskites. II. Structure stabilizing forces. *Acta Crystallogr. B* **53**, 44–66 (1997).

12. Glazer, A. M. The classification of tilted octahedra in perovskites. *Acta Crystallogr. B* **28**, 3384–3392 (1972).

13. Woodward, P. M. Octahedral tilting in perovskites. I. Geometrical considerations. *Acta Crystallogr. B* **53**, 32–43 (1997).

14. Howard, C. J. & Stokes, H. T. Group-theoretical analysis of octahedral tilting in perovskites. *Acta Crystallogr. B* **54**, 782–789 (1998).

15. Duyker, S. G., Hill, J. A., Howard, C. J. & Goodwin, A. L. Guest-activated forbidden tilts in a molecular perovskite analogue. *J. Am. Chem. Soc.* **138**, 11121–11123 (2016).

16. Boström, H. L. B., Hill, J. A. & Goodwin, A. L. Columnar shifts as symmetry-breaking degrees of freedom in molecular perovskites. *Phys. Chem. Chem. Phys.* **18**, 31881–31894 (2016).

17. Li, H., Eddaoudi, M., O'Keeffe, M. & Yaghi, O. M. Design and synthesis of an exceptionally stable and highly porous metal-organic framework. *Nature* **402**, 276–279 (1999).

18. Zheng, H. *et al.* Nanostructured tungsten oxide - properties, synthesis, and applications. *Adv. Funct. Mater.* **21**, 2175–2196 (2011).

19. Ferretti, A., Rogers, D. B. & Goodenough, J. B. The relation of the electrical conductivity in single crystals of rhenium trioxide to the conductivities of Sr_2MgReO_6 and $NaxWO_3$. *J. Phys. Chem. Solids* **26**, 2007–2011 (1965).

20. Mattheiss, L. F. Band Structure and Fermi Surface of ReO_3. *Phys. Rev.* **181**, 987–1000 (1969).

21. Tanisaki, S. Crystal structure of monoclinic tungsten trioxide at room temperature. *J. Phys. Soc. Jpn.* **15**, 573–581 (1960).

22. Honig, J. M., Dimmock, J. O. & Kleiner, W. H. ReO_3 band structure in the tight-binding approximation. *J. Chem. Phys.* **50**, 5232–5242 (1969).

23. Sleight, A. & Gillson, J. Preparation and properties of alkali rhenium bronzes and a WO_3 - ReO_3 solid solution. *Solid State Commun.* **4**, 601–602 (1966).

24. Chatterji, T., Hansen, T. C., Brunelli, M. & Henry, P. F. Negative thermal expansion of ReO_3 in the extended temperature range. *Appl. Phys. Lett.* **94**, 241902 (2009).

25. Purans, J. *et al.* X-ray absorption spectroscopy study of local dynamics and thermal expansion in ReO_3. *Phys. Rev. B* **92**, 014302 (2015).

26. Takenaka, K. Negative thermal expansion materials: Technological key for control of thermal expansion. *Sci. Technol. Adv. Mater.* **13** (2012).

27. Rodriguez, E. E. *et al.* The role of static disorder in negative thermal expansion in ReO_3. *J. Appl. Phys.* **105**, 114901 (2009).

28. Lind, C. Two decades of negative thermal expansion research: Where do we stand? *Materials* **5**, 1125–1154 (2012).

29. Corà, F., Stachiotti, M. G., Catlow, C. R. A. & Rodriguez, C. O. Transition metal oxide chemistry: Electronic structure study of WO_3, ReO_3, and $NaWO_3$. *J. Chem. Phys. B* **101**, 3945–3952 (1997).

30. Bozin, E. S., Chatterji, T. & Billinge, S. J. L. Local structure of ReO_3 at ambient pressure from neutron total-scattering study. *Phys. Rev. B* **86**, 3–6 (2012).

31. Jo/rgensen, J.-E., Jorgensen, J. D., Batlogg, B., Remeika, J. P. & Axe, J. D. Order parameter and critical exponent for the pressure-induced phase transitions in reo_3. *Phys. Rev. B* **33**, 4793–4798 (1986).

32. Schirber, J. E. & Morosin, B. "Compressibility Collapse" Transition in ReO_3. *Phys. Rev. Lett.* **42**, 1485–1487 (1979).

33. Biswas, K. *et al.* Pressure-induced phase transitions in nanocrystalline ReO_3. *J. Phys. Condens. Matter.* **19** (2007).

34. Muthu, D. V. S. *et al.* Pressure-induced structural phase transitions and phonon anomalies in ReO_3 : Raman and first-principles study. *Phys. Rev. B* **91**, 224308 (2015).

35. Cava, R., Santoro, A., Murphy, D., Zahurak, S. & Roth, R. The structures of lithium-inserted metal oxides: $LiReO_3$ and Li_2ReO_3. *J. Solid State Chem.* **42**, 251–262 (1982).

36. Cava, R., Santoro, A., Murphy, D., Zahurak, S. & Roth, R. The structures of the lithium inserted metal oxides $Li_{0.2}ReO_3$ and $Li_{0.36}WO_3$. *J. Solid State Chem.* **50**, 121–128 (1983).

37. Bashian, N. H. *et al.* Correlated polyhedral rotations in the absence of polarons during electrochemical insertion of lithium in ReO_3. *ACS Energy Lett.* **3**, 2513–2519 (2018).

38. Santato, C., Odziemkowski, M., Ulmann, M. & Augustynski, J. Crystallographically oriented mesoporous WO_3 films: Synthesis, characterization, and applications. *J. Am. Chem. Soc.* **123**, 10639–10649 (2001).

39. Cronin, J., Tarico, D., Tonazzi, J., Agrawal, A. & Kennedy, S. Microstructure and properties of sol-gel deposited WO_3 coatings for large area electrochromic windows. *Sol. Energy Mater. Sol. Cells* **29**, 371–386 (1993).

40. Sun, M., Xu, N., Cao, Y. W., Yao, J. N. & Wang, E. G. Nanocrystalline tungsten oxide thin film: Preparation, microstructure, and photochromic behavior. *J. Mater. Sci.* **15**, 927–933 (2000).

41. Lee, S.-H. *et al.* Crystalline WO_3 nanoparticles for highly improved electrochromic applications. *Adv. Mater.* **18**, 763–766 (2006).

42. Baeck, S.-H., Choi, K.-S., Jaramillo, T., Stucky, G. & McFarland, E. Enhancement of photocatalytic and electrochromic properties of electrochemically fabricated mesoporous WO_3 thin films. *Adv. Mater.* **15**, 1269–1273 (2003).

43. Aird, A. & Salje, E. K. H. Sheet superconductivity in twin walls: experimental evidence of. *J. Phys. Condens. Matter.* **10**, L377–L380 (1998).

44. Wang, L., Teleki, A., Pratsinis, S. E. & Gouma, P. I. Ferroelectric WO_3 nanoparticles for acetone selective detection. *Chem. Mater.* **20**, 4794–4796 (2008).

45. Antonik, M. *et al.* Microstructural effects in WO_3 gas-sensing films. *Thin Solid Films* **256**, 247–252 (1995).

46. Galatsis, K., Li, Y., Wlodarski, W. & Kalantar-zadeh, K. Solgel prepared MoO_3-WO_3 thin-films for O_2 gas sensing. *Sensor Actuat. B-Chem* **77**, 478–483 (2001).

47. Li, X.-L., Lou, T.-J., Sun, X.-M. & Li, Y.-D. Highly sensitive WO_3 hollow-sphere gas sensors. *Inorg. Chem.* **43**, 5442–5449 (2004).

48. Ponzoni, A., Comini, E., Ferroni, M. & Sberveglieri, G. Nanostructured WO_3 deposited by modified thermal evaporation for gas-sensing applications. *Thin Solid Films* **490**, 81–85 (2005).

49. Zheng, H. *et al.* Nanostructured tungsten oxide - properties, synthesis, and applications. *Adv. Funct. Mater.* **21**, 2175–2196 (2011).

50. Ma, M. *et al.* Dual oxygen and tungsten vacancies on a WO_3 photoanode for enhanced water oxidation. *Angew. Chem. Int. Ed.* **55**, 11819–11823 (2016).

51. Zhang, J., Liu, Z. & Liu, Z. Novel WO_3/Sb_2S_3 heterojunction photocatalyst based on WO_3 of different morphologies for enhanced efficiency in photoelectrochemical water splitting. *ACS Appl. Mater. Interfaces* **8**, 9684–9691 (2016).

52. Li, W. *et al.* WO_3 nanoflakes for enhanced photoelectrochemical conversion. *ACS Nano* **8**, 11770–11777 (2014).

53. Hou, Y., Zuo, F., Dagg, A. P., Liu, J. & Feng, P. Branched WO_3 nanosheet array with layered C_3N_4 heterojunctions and CoO_x nanoparticles as a flexible photoanode for efficient photoelectrochemical water oxidation. *Adv. Mater.* **26**, 5043–5049 (2014).

54. Su, J., Feng, X., Sloppy, J. D., Guo, L. & Grimes, C. A. Vertically aligned WO_3 nanowire arrays grown directly on transparent conducting oxide coated glass: Synthesis and photoelectrochemical properties. *Nano Lett.* **11**, 203–208 (2011).

55. Li, N. *et al.* Aqueous synthesis and visible-light photochromism of metastable h-WO_3 hierarchical nanostructures. *Eur. J. Inorg. Chem.* **2015**, 2804–2812 (2015).

56. Chen, Z. *et al.* Hierarchical nanostructured WO_3 with biomimetic proton channels and mixed ionic-electronic conductivity for electrochemical energy storage. *Nano Lett.* **15**, 6802–6808 (2015).

57. Yoon, S. *et al.* Development of a high-performance anode for lithium ion batteries using novel ordered mesoporous tungsten oxide materials with high electrical conductivity. *Phys. Chem. Chem. Phys.* **13**, 11060 (2011).

58. Girish Kumar, S. & Koteswara Rao, K. Tungsten-based nanomaterials (WO_3 & Bi_2WO_6): Modifications related to charge carrier transfer mechanisms and photocatalytic applications. *App. Surf. Sci.* **355**, 939–958 (2015).

59. Kida, T. *et al.* WO_3 nanolamella gas sensor: Porosity control using SnO_2 nanoparticles for enhanced NO_2 sensing. *Langmuir* **30**, 2571–2579 (2014).

60. Amano, F., Ishinaga, E. & Yamakata, A. Effect of particle size on the photocatalytic activity of WO_3 particles for water oxidation. *J. Phys. Chem. C* **117**, 22584–22590 (2013).

61. Chen, D. & Ye, J. Hierarchical WO_3 hollow shells: Dendrite, sphere, dumbbell, and their photocatalytic properties. *Adv. Funct. Mater.* **18**, 1922–1928 (2008).

62. Wang, H., Dong, X., Peng, S., Dong, L. & Wang, Y. Improvement of thermoelectric properties of WO_3 ceramics by ZnO addition. *J. Alloys Compd.* **527**, 204–209 (2012).

63. Kieslich, G. *et al.* Using crystallographic shear to reduce lattice thermal conductivity: high temperature thermoelectric characterization of the spark plasma sintered Magnéli phases $WO_{2.90}$ and $WO_{2.722}$. *Phys. Chem. Chem. Phys.* **15**, 15399 (2013).

64. Kim, S.-J. *et al.* Mesoporous WO_3 nanofibers with protein-templated nanoscale catalysts for detection of trace biomarkers in exhaled breath. *ACS Nano* **10**, 5891–5899 (2016).

65. Shendage, S. *et al.* Sensitive and selective NO_2 gas sensor based on WO_3 nanoplates. *Sensor Actuat. B-Chem* **240**, 426–433 (2017).

66. Rao, P. M. *et al.* Simultaneously efficient light absorption and charge separation in WO_3/$BiVO_4$ core/shell nanowire photoanode for photoelectrochemical water oxidation. *Nano Lett.* **14**, 1099–1105 (2014).

67. Tordjman, M., Weinfeld, K. & Kalish, R. Boosting surface charge-transfer doping efficiency and robustness of diamond with WO_3 and ReO_3. *Appl. Phys. Lett.* **111**, 111601 (2017).

68. Kim, Y., Wieder, B. J., Kane, C. L. & Rappe, A. M. Dirac line nodes in inversion-symmetric crystals. *Phys. Rev. Lett.* **115**, 036806 (2015).

69. Juza, R. & Hahn, H. Über die kristallstrukturen von Cu_3N, GaN und InN metallamide und metallnitride. *Z. Anorg. Allg. Chem.* **239**, 282–287 (1938).

70. Paniconi, G. *et al.* Structural chemistry of Cu_3N powders obtained by ammonolysis reactions. *Solid State Sci.* **9**, 907–913 (2007).

71. Zhao, J., You, S., Yang, L. & Jin, C. Structural phase transition of Cu_3N under high pressure. *Solid State Commun.* **150**, 1521–1524 (2010).

72. Birkett, M. *et al.* Atypically small temperature-dependence of the direct band gap in the metastable semiconductor copper nitride Cu_3N. *Phys. Rev. B* **95**, 115201 (2017).

73. Terada, S., Tanaka, H. & Kubota, K. Heteroepitaxial growth of Cu_3N thin films. *J. Cryst. Growth* **94**, 567–568 (1989).

74. Asano, M., Umeda, K. & Tasaki, A. Cu_3N thin film for a new light recording media. *Jpn. J. Appl. Phys.* **29**, 1985–1986 (1990).

75. Juza, R. & Hahn, H. Kupfernitrid metallamide und metallnitride. VII. *Z. Anorg. Allg. Chem.* **241**, 172–178 (1939).

76. Zakutayev, A. *et al.* Defect tolerant semiconductors for solar energy conversion. *J. Phys. Chem. Lett.* **5**, 1117–1125 (2014).

77. Pereira, N., Dupont, L., Tarascon, J. M., Klein, L. C. & Amatucci, G. G. Electrochemistry of Cu_3N with lithium. *J. Electrochem. Soc.* **150**, A1273 (2003).

78. Wu, H. & Chen, W. Copper nitride nanocubes: Size-controlled synthesis and application as cathode catalyst in alkaline fuel cells. *J. Am. Chem. Soc.* **133**, 15236–15239 (2011).

79. Fischer, D. & Jansen, M. Synthesis and structure of Na_3N. *Angew. Chem. Int. Ed.* **41**, 1755–1756 (2002).

80. Vajenine, G. V. Plasma-assisted synthesis andpProperties of Na_3N. *Inorg. Chem.* **46**, 5146–5148 (2007).

81. Vajenine, G. V., Hoch, C., Dinnebier, R. E., Senyshyn, A. & Niewa, R. A temperature-dependent structural study of anti-ReO_3 -type Na_3N: to distort or not to distort? *Z. Anorg. Allg. Chem.* **636**, 94–99 (2010).

82. Kim, D. *et al.* Type-II Dirac line node in strained Na_3N. *Phys. Rev. Mater.* **2**, 104203 (2018).

83. Zintl, E. & Brauer, G. Konstitution des lithiumnitrids. *Z. Elektrochem.* **41**, 102–107 (1935).

84. Fischer, D., Cancarevic, Z., Schön, J. C. & Jansen, M. Zur synthese und struktur von K_3N. *Z. Anorg. Allg. Chem.* **630**, 156–160 (2004).

85. Greve, B. K. *et al.* Pronounced negative thermal expansion from a simple structure: Cubic ScF_3. *J. Am. Chem. Soc.* **132**, 15496–15498 (2010).

86. Groult, H. *et al.* Nano-CoF_3 prepared by direct fluorination with F_2 gas: Application as electrode material in Li-ion battery. *J. Flouruine Chem.* **196**, 117–127 (2017).

87. Chaudhuri, S., Chupas, P. J., Wilson, M., Madden, P. & Grey, C. P. Study of the nature and mechanism of the rhombohedral-to-cubic phase transition in α-AlF_3 with molecular dynamics simulations. *J. Phys. Chem. B* **108**, 3437–3445 (2004).

88. Hepworth, M. A., Jack, K. H., Peacock, R. D. & Westland, G. J. The crystal structures of the trifluorides of iron, cobalt, ruthenium, rhodium, palladium and iridium. *Acta Crystallogr.* **10**, 63–69 (2002).

89. Daniel, P., Bulou, A., Leblanc, M., Rousseau, M. & Nouet, J. Structural and vibrational study of VF_3. *Mater. Res. Bull.* **25**, 413–420 (1990).

90. Siegel, S. The structure of TiF_3. *Acta Crystallogr.* **9**, 684–684 (1956).

91. Shannon, R. D. T. & Prewitt, C. T. Effective ionic radii in oxides and fluorides. *Acta Crystallogr. B* **25**, 925–946 (1969).

92. Shannon, R. D. Revised effective ionic radii and systematic studies of interatomic distances in halides and chalcogenides. *Acta Crystallogr. A* **32**, 751–767 (1976).

93. Hu, L. *et al.* New insights into the negative thermal expansion : Direct experimental evidence for the “Guitar-String” effect in cubic ScF_3. *J. Am. Chem. Soc.* **138**, 8320–8323 (2016).

94. Piskunov, S. *et al.* Interpretation of unexpected behavior of infrared absorption spectra of ReO_3 beyond the quasiharmonic approximation. *Phys. Rev. B* **93**, 214101 (2016).

95. Bhandia, R., Siegrist, T., Besara, T. & Schmiedeshoff, G. M. Grüneisen divergence near the structural quantum phase transition in ScF 3. *Philos. Mag.* **99**, 631–643 (2019).

96. Yang, C. *et al.* Size effects on negative thermal expansion in cubic ScF_3. *Appl. Phys. Lett.* **109**, 023110 (2016).

97. Hu, L. *et al.* Localized symmetry breaking for tuning thermal expansion in ScF_3 nanoscale frameworks. *J. Am. Chem. Soc.* **140**, 4477–4480 (2018).

98. Wang, T. *et al.* Tunable thermal expansion and magnetism in Zr-doped ScF_3. *Appl. Phys. Lett.* **109**, 181901 (2016).

99. Chen, J. *et al.* Tunable thermal expansion in framework materials through redox intercalation. *Nat. Commun.* **8**, 14441 (2017).

100. Goodwin, A. L., Chapman, K. W. & Kepert, C. J. Guest-dependent negative thermal expansion in nanoporous Prussian Blue analogues $M^{II}Pt^{IV}(CN)_6 \bullet xH_2O$ ($0 \leq X \leq 2$; M = Zn, Cd). *J. Am. Chem. Soc.* **127**, 17980–17981 (2005).

101. Duan, N., Kameswari, U. & Sleight, A. W. Further Contraction of ZrW_2O_8. *J. Am. Chem. Soc.* **121**, 10432–10433 (2002).

102. Phillips, A. E., Goodwin, A. L., Halder, G. J., Southon, P. D. & Kepert, C. J. Nanoporosity and exceptional negative thermal expansion in single-network cadmium cyanide. *Angew. Chem. Inter. Ed.* **47**, 1396–1399 (2008).

103. Phillips, A. E., Halder, G. J., Chapman, K. W., Goodwin, A. L. & Kepert, C. J. Zero thermal expansion in a flexible, stable framework: tetramethylammonium copper(I) zinc(II) cyanide. *J. Am. Chem. Soc.* **132**, 10–11 (2010).

104. Carey, T., Tang, C. C., Hriljac, J. A. & Anderson, P. A. Chemical control of thermal expansion in cation-exchanged zeolite A. *Chem. Mater.* **26**, 1561–1566 (2014).

105. Arai, H., Okada, S., Sakurai, Y. & Yamaki, J. I. Cathode performance and voltage estimation of metal trihalides. *J. Power Sources* **68**, 716–719 (1997).

106. Nishijima, M. *et al.* Cathode properties of metal trifluorides in Li and Na secondary batteries. *J. Power Sources* **190**, 558–562 (2009).

107. Zhou, M., Zhao, L., Doi, T., Okada, S. & ichi Yamaki, J. Thermal stability of FeF_3 cathode for Li-ion batteries. *J. Power Sources* **195**, 4952–4956 (2010).

108. Takami, T. *et al.* Role of the particle size of Fe nanoparticles in the capacity of FeF_3 batteries. *AIP Adv.* **9**, 045301 (2019).

109. Yang, Z. *et al.* Atomistic insights into FeF_3 nanosheet: An ultrahigh-rate and long-life cathode material for Li-ion batteries. *ACS Appl. Mater. Interfaces* **10**, 3142–3151 (2018).

110. Jiang, J., Li, L., Xu, M., Zhu, J. & Li, C. M. FeF_3•thin nickel ammine nitrate matrix: smart configurations and applications as superior cathodes for Li-ion batteries. *ACS Appl. Mater. Interfaces* **8**, 16240–16247 (2016).

111. Kim, T. *et al.* A cathode material for lithium-ion batteries based on graphitized carbon-wrapped FeF_3 nanoparticles prepared by facile polymerization. *J. Mater. Chem.* **4**, 14857–14864 (2016).

112. Li, C., Gu, L., Tsukimoto, S., van Aken, P. A. & Maier, J. Low-temperature ionic-liquid-based synthesis of nanostructured iron-based fluoride cathodes for lithium batteries. *Adv. Mater.* **22**, 3650–3654 (2010).

113. Yang, Z., Pei, Y., Wang, X., Liu, L. & Su, X. First principles study on the structural, magnetic and electronic properties of Co-doped FeF_3. *Comput. Theor. Chem.* **980**, 44–48 (2012).

114. Liu, L. *et al.* Excellent cycle performance of Co-doped FeF_3/C nanocomposite cathode material for lithium-ion batteries. *J. Mater. Chem.* **22**, 17539 (2012).

115. Liu, L. *et al.* A comparison among FeF_3•$3H_2O$, FeF_3•$0.33H_2O$ and FeF_3 cathode materials for lithium ion batteries: Structural, electrochemical, and mechanism studies. *J. Power Sources* **238**, 501–515 (2013).

116. Kitajou, A. *et al.* Novel synthesis and electrochemical properties of perovskite-type $NaFeF_3$ for a sodium-ion battery. *J. Power Sources* **198**, 389–392 (2012).

117. Ruchaud, N., Mirambet, C., Fournes, L., Grannec, J. & Soubeyroux, J. L. Determination of the cationic arrangement in Sn_2F_6 from neutron powder diffraction. *Z. Anorg. Allg. Chem.* **590**, 173–180 (1990).

118. Köhl, P., Reinen, D., Decher, G. & Wanklyn, B. Strukturelle modifikationen von $FeZrF_6$. *Z. Kristallogr. Cryst. Mater.* **153**, 211–220 (1980).

119. Mayer, H., Reinen, D. & Heger, G. Struktur und bindung in übergangsmetall-fluoriden $M^{II}Me^{IV}F_6$. *J. Solid State Chem.* **50**, 213–224 (1983).

120. Bachmann, B. & Müller, B. G. Zur synthese und kristallstruktur von $LiPdAlF_6$ und $PdZrF_6$. *Z. Anorg. Allg. Chem* **619**, 189–192 (1993).

121. Rodriguez, V. & Couzi, M. Structural phase transition in the ordered fluorides $M^{II}ZrF_6$ (M^{II} = Co, Zn). III. Landau theory. *J. Phys. Condens. Matter* **2**, 7395–7406 (1990).

122. Gerasimenko, A. V., Gaivoronskaya, K. A., Slobodyuk, A. B. & Didenko, N. A. Magnesium Hexafluoridozirconates $MgZrF_6 \bullet 5H_2O$, $MgZrF_6 \bullet 2H_2O$, and $MgZrF_6$: Structures, phase transitions, and internal mobility of water molecules. *Z. Anorg. Allg. Chem* **643**, 1785–1792 (2017).

123. Friebel, C., Pebler, J., Steffens, F., Weber, M. & Reinen, D. Phase transitions in $CuZrF_6$ and $CrZrF_6$: A Mössbauer and EPR study of local and cooperative Jahn-Teller distortions. *J. Solid State Chem.* **46**, 253–264 (1983).

124. Schmidt, R., Kraus, M. & Müller, B. G. Neue fluorozirconate und -hafnate mit V2+ und Ti2+. *Z. Anorg. Allg. Chem.* **627**, 2344–2350 (2001).

125. Le Mercier, T., Chassaing, J., Bizot, D. & Quarton, M. Structural, spectroscopic and magnetic studies of $V^{II}M^{IV}F_6$ compounds with M^{IV} = Zr, Nb. *Mater. Res. Bull* **27**, 259–267 (1992).

126. Hester, B. R., dos Santos, A. M., Molaison, J. J., Hancock, J. C. & Wilkinson, A. P. Synthesis of defect perovskites $(He_{2-x}square_x)(CaZr)F_6$ by inserting helium into the negative thermal expansion material $CaZrF_6$. *J. Am. Chem. Soc.* **139**, 13284–13287 (2017).

127. De, I., Desai, V. P. & Chakravarty, A. S. Magnetic Properties of Some Complexes of Mo^{5+}. *Phys. Rev. B* **8**, 3769–3772 (1973).

128. Llorente, S. *et al.* Synthesis and crystal structure of $Cu^{II}Mo^{IV}F_6$ and $Cr^{II}Nb^{IV}F_6$ (LT Form). *Z. Anorg. Allg. Chem* **624**, 1538–1542 (1998).

129. Goubard, F. *et al.* Fluorocomplexes of niobium IV: the magnetic structure of $VNbF_6$. *J. Magn. Magn. Mater.* **146**, 129–132 (1995).

130. Yang, C. *et al.* Large positive thermal expansion and small band gap in double-ReO_3-type compound $NaSbF_6$. *Inorg. Chem.* **56**, 4990–4995 (2017).

131. Gupta, M. K., Singh, B., Mittal, R. & Chaplot, S. L. Negative thermal expansion behavior in ReO_3. *Phys. Rev. B* **98**, 014301 (2018).

132. Hancock, J. C. *et al.* Large negative thermal expansion and anomalous behavior on compression in cubic ReO_3-type $A^{II}B^{IV}F_6$: $CaZrF_6$ and $CaHfF_6$. *Chem. Mater.* **27**, 3912–3918 (2015).

133. Ticknor, J. O. *et al.* Zero thermal expansion and abrupt amorphization on compression in anion excess ReO_3-type cubic $YbZrF_7$. *Chem. Mater.* **30**, 3071–3077 (2018).

134. Baxter, S. J., Hester, B. R., Wright, B. R. & Wilkinson, A. P. Controlling the Negative Thermal Expansion and Response to Pressure in ReO_3-type fluorides by the deliberate introduction of excess fluoride: $Mg_{1-x}Zr_{1+x}F_{6+2x}$, x = 0.15, 0.30, 0.40, and 0.50. *Chem. Mater.* acs.chemmater.9b00592 (2019).

135. Reddy, M., Madhavi, S., Subba Rao, G. & Chowdari, B. Metal oxyfluorides $TiOF_2$ and NbO_2F as anodes for Li-ion batteries. *J. Power Sources* **162**, 1312–1321 (2006).

136. Pérez-Flores, J. C. *et al.* VO_{2F}: a new transition metal oxyfluoride with high specific capacity for Li ion batteries. *J. Mater. Chem. A* **3**, 20508–20515 (2015).

137. Frevel, L. K. & Rinn, H. W. The crystal structure of NbO_2F and TaO_2F. *Acta Crystallogr.* **9**, 626–627 (1956).

138. Poulain, M., Lucas, J. & Tilley, R. J. A structural study of a nonstoichiometric niobium-zirconium oxyfluoride with the ReO_3 type structure. *J. Solid State Chem.* **17**, 331–337 (1976).

139. Pierce, J. W. & Vlasse, M. The crystal structures of two oxyfluorides of molybdenum. *Acta Crystallogr. B* **27**, 158–163 (1971).

140. Nakhal, S. & Lerch, M. New transition metal oxide fluorides with ReO_3-type structure. *Z. Naturforsch. B Chem. Sci.* **71**, 457–461 (2016).

141. Nakhal, S., Bredow, T. & Lerch, M. Syntheses and crystal structures of New ReO_3-type-derived transition metal oxide fluorides. *Z. Anorg. Allg. Chem.* **641**, 1036–1042 (2015).

142. Dabachi, J., Body, M., Galven, C., Boucher, F. & Legein, C. Preparation-dependent composition and O/F ordering in NbO_2F and TaO_2F. *Inorg. Chem.* **56**, 5219–5232 (2017).

143. Cambaz, M. A. *et al.* Vanadium oxyfluoride/few-layer graphene composite as a high-performance cathode material for lithium batteries. *Inorg. Chem.* **55**, 3789–3796 (2016).

144. Chen, R. *et al.* Lithiation-driven structural transition of VO_2F into disordered rock-salt Li_xVO_2F. *RSC Adv.* **6**, 65112–65118 (2016).

145. Wang, X. *et al.* Structural changes in a high-energy density VO_2F cathode upon heating and Li cycling. *ACS Appl. Mater. Interfaces* **1**, 4514–4521 (2018).

146. Mitchell, R. H., Welch, M. D. & Chakhmouradian, A. R. Nomenclature of the perovskite supergroup: A hierarchical system of classification based on crystal structure and composition. *Mineral. Mag.* **81**, 411–461 (2017).

147. Xue, X. & Kanzaki, M. High-pressure δ-$Al(OH)_3$ and δ-AlOOH phases and isostructural hydroxides/oxyhydroxides: New structural insights from high-resolution ^{1}H and ^{27}Al NMR. *J. Phys. Chem. B* **111**, 13156–13166 (2007).

148. Welch, M. D. & Kleppe, A. K. Polymorphism of the hydroxide perovskite $Ga(OH)_3$ and possible proton-driven transformational behaviour. *Phys. Chem. Miner.* **43**, 515–526 (2016).

149. Au-Yeung, S. C. F., Denes, G., Greedan, J. E., Eaton, D. R. & Birchall, T. A novel synthetic route to "iron trihydroxide, $Fe(OH)_3$": characterization and magnetic properties. *Inorg. Chem.* **23**, 1513–1517 (1984).

150. Au-Yeung, S. C. F. *et al.* The preparation and characterization of iron trihydroxide, $Fe(OH)_3$. *Can. J. Chem.* **63**, 3378–3385 (1985).

151. Schubert, K. & Seitz, A. Kristallstruktur von $Sc(OH)_3$ und $In(OH)_3$. *Z. Anorg. Allg. Chem.* **256**, 226–238 (1948).

152. Mullica, D., Beall, G., Milligan, W., Korp, J. & Bernal, I. The crystal structure of cubic $In(OH)_3$ by X-ray and neutron diffraction methods. *J. Inorg. Nucl. Chem. Lett.* **41**, 277–282 (1979).

153. Mullica, D. & Milligan, W. Structural refinement of cubic $Lu(OH)_3$. *J. Inorg. Nucl. Chem.* **42**, 223–227 (1980).

154. Mullica, D., Sappenfield, E., Gable, D. & Tims, T. Crystal structural analyses of 1:3 (Lu, In)$(OH)_3$ and 1:3 (Yb, In)$(OH)_3$. *J. Less. Common Met.* **152**, 157–163 (1989).

155. Birch, W. D., Pring, A., Reller, A. & Schmalle, H. Bernalite: a new ferric hydroxide with perovskite structure. *Naturwissenschaften* **79**, 509–511 (1992).

156. Li, B. *et al.* In_2O_3 hollow microspheres: Synthesis from designed $In(OH)_3$ precursors and applications in gas sensors and photocatalysis. *Langmuir* **22**, 9380–9385 (2006).

157. Morgenstern-Badarau, I. Effet Jahn-Teller et structure cristalline de l'hydroxyde $CuSn(OH)_6$. *J. Solid State Chem.* **17**, 399–406 (1976).

158. Neilson, J. R., Kurzman, J. A., Seshadri, R. & Morse, D. E. Ordering double perovskite hydroxides by kinetically controlled aqueous hydrolysis. *Inorg. Chem.* **50**, 3003–3009 (2011).

159. Mizoguchi, H., Bhuvanesh, N. S. P., Kim, Y.-I., Ohara, S. & Woodward, P. M. Hydrothermal crystal growth and structure determination of double hydroxides $LiSb(OH)_6$, $BaSn(OH)_6$, and $SrSn(OH)_6$. *Inorg. Chem.* **53**, 10570–10577 (2014).

160. Nakayama, N., Kosuge, K., Kachi, S., Shinjo, T. & Takada, T. Magnetic properties of $FeSn(OH)_6$ and its oxidation product, $FeSnO(OH)_5$. *Mater. Res. Bull.* **13**, 17–22 (1978).

161. Xu, R., Deng, B., Min, L., Xu, H. & Zhong, S. $CuSn(OH)_6$ submicrospheres: Room-temperature synthesis and weak antiferromagnetic behavior. *Mater. Lett.* **65**, 733–735 (2010).

162. Wu, J. M. & Chen, Y. N. The surface plasmon resonance effect on the enhancement of photodegradation activity by Au/$ZnSn(OH)_6$ nanocubes. *Dalton Trans.* **44**, 16294–16303 (2015).

163. Wang, L. *et al.* Single-crystalline $ZnSn(OH)_6$ hollow cubes via self-templated synthesis at room temperature and their photocatalytic properties. *J. Mater. Chem.* **21**, 4352 (2011).

164. Gao, Y. *et al.* Perovskite hydroxide $CoSn(OH)_6$ nanocubes for efficient photoreduction of CO_2 to CO. *ACS Sustain. Chem. Eng.* **6**, 781–786 (2018).

165. Chen, D. *et al.* Preferential cation vacancies in perovskite hydroxide for the oxygen evolution reaction. *Angew. Chem. Int. Ed.* **57**, 8691–8696 (2018).

166. Li, B.-Q., Tang, C., Wang, H.-F., Zhu, X.-L. & Zhang, Q. An aqueous preoxidation method for monolithic perovskite electrocatalysts with enhanced water oxidation performance. *Sci. Adv.* **2**, e1600495 (2016).

167. Welch, M. D., Crichton, W. A. & Ross, N. L. Compression of the perovskite-related mineral bernalite $Fe(OH)_3$ to 9 GPa and a reappraisal of its structure. *Mineral. Mag.* **69**, 309–315 (2005).

168. Oftedal, I. XXXIII. Die kristallstruktur von skutterudit und speiskobalt-chloanthit. *Z. Kristallogr. Cryst. Mater.* **66**, 517–546 (1928).

169. Mandel, N. & Donohue, J. The refinement of the crystal structure of skutterudite, $CoAs_3$. *Acta Crystallogr. B* **27**, 2288–2289 (1971).

170. von Schnering, H. G. Homoatomic bonding of main group elements. *Angew. Chem. Int. Ed.* **20**, 33–51 (1981).

171. Jeitschko, W. & Braun, D. $LaFe_4P_{12}$ with filled $CoAs_3$-type structure and isotypic lanthanoid-transition metal polyphosphides. *Acta Crystallogr. B* **33**, 3401–3406 (1977).

172. Meisner, G. Superconductivity and magnetic order in ternary rare earth transition metal phosphides. *Physica C* **108**, 763–764 (1981).

173. Sales, B. C., Mandrus, D. & Williams, R. K. Filled skutterudite antimonides: A new class of thermoelectric materials. *Science* **272**, 1325–1328 (1996).

174. Caillat, T., Borshchevsky, A. & Fleurial, J. Properties of single crystalline semiconducting $CoSb_3$. *J. Appl. Phys.* **80**, 4442–4449 (1996).

175. Snyder, G. J. & Toberer, E. S. Complex thermoelectric materials. *Nat. Mater.* **7**, 105–114 (2008).

176. Gaultois, M. W. *et al.* Data-driven review of thermoelectric materials: Performance and resource considerations. *Chem. Mater.* **25**, 2911–2920 (2013).

177. Shi, X. *et al.* Multiple-filled skutterudites: High thermoelectric figure of merit through separately optimizing electrical and thermal transports. *J. Am. Chem. Soc.* **133**, 7837–7846 (2011).

178. Khan, A. U. *et al.* Nano-micro-porous skutterudites with 100% enhancement in ZT for high performance thermoelectricity. *Nano Energy* **31**, 152–159 (2017).

179. Buser, H. J., Schwarzenbach, D., Petter, W. & Ludi, A. The crystal structure of Prussian Blue: $Fe_4[Fe(CN)_6]_3.xH_2O$. *Inorg. Chem.* **16**, 2704–2710 (1977).

180. Chapman, K. W., Chupas, P. J. & Kepert, C. J. Compositional dependence of negative thermal expansion in the prussian blue analogues $M^{II}Pt^{IV}(CN)_6$ (M = Mn, Fe, Co, Ni, Cu, Zn, Cd). *J. Am. Chem. Soc.* **128**, 7009–7014 (2006).

181. Gao, Q. *et al.* Low-frequency phonon driven negative thermal expansion in cubic $GaFe(CN)_6$ prussian blue analogues. *Inorg. Chem.* **57**, 10918–10924 (2018).

182. Behera, J. N., D'Alessandro, D. M., Soheilnia, N. & Long, J. R. Synthesis and characterization of ruthenium and ironruthenium Prussian blue analogues. *Chem. Mater.* **21**, 1922–1926 (2009). URL https://pubs.acs.org/doi/10.1021/cm900230p.

183. Yang, J., Wang, H., Lu, L., Shi, W. & Zhang, H. Large-scale synthesis of Berlin Green $Fe[Fe(CN)_6]$ microcubic crystals. *Cryst. Growth Des.* **6**, 2438–2440 (2006).

184. Gao, Q. *et al.* Switching between giant positive and negative thermal expansions of a $YFe(CN)_6$-based Prussian Blue analogue induced by guest species. *Angew. Chem. Int. Ed.* **56**, 9023–9028 (2017).

185. Kumar, A., Yusuf, S. M. & Keller, L. Structural and magnetic properties of $Fe[Fe(CN)_6]\bullet 4H_2O$. *Phys. Rev. B* **71**, 054414 (2005).

186. Ohba, M. & kawa, H. Synthesis and magnetism of multi-dimensional cyanide-bridged bimetallic assemblies. *Coordin. Chem. Rev.* **198**, 313–328 (2000).

187. Ferlay, S., Mallah, T., Ouahès, R., Veillet, P. & Verdaguer, M. A room-temperature organometallic magnet based on Prussian blue. *Nature* **378**, 701–703 (1995).

188. Ohkoshi, S. I., Arai, K. I., Sato, Y. & Hashimoto, K. Humidity-induced magnetization and magnetic pole inversion in a cyano-bridged metal assembly. *Nat. Mater.* **3**, 857–861 (2004).

189. Lu, Y., Wang, L., Cheng, J. & Goodenough, J. B. Prussian blue: a new framework of electrode materials for sodium batteries. *Chem. Commun.* **48**, 6544 (2012).

190. Zhang, J. *et al.* $FeFe(CN)_6$ nanocubes as a bipolar electrode material in aqueous symmetric sodium-ion batteries. *Chem. Plus. Chem.* **82**, 1170–1173 (2017).

191. Wu, X. *et al.* Single-crystal $FeFe(CN)_6$ nanoparticles: a high capacity and high rate cathode for Na-ion batteries. *J. Mater. Chem. A* **1**, 10130 (2013).

192. Wu, X. *et al.* Low defect $FeFe(CN)_6$ framework as stable host material for high performance Li-ion batteries. *ACS Appl. Mater. Interfaces* **8**, 23706–23712 (2016).

193. Shadike, Z. *et al.* Long life and high-rate Berlin green $FeFe(CN)_6$ cathode material for a non-aqueous potassium-ion battery. *J. Mater. Chem. A* **5**, 6393–6398 (2017).

194. Cliffe, M. J. *et al.* Strongly coloured thiocyanate frameworks with perovskite-analogue structures. *Chem. Sci.* **10**, 793–801 (2019).

195. Ravnsbæk, D. B. *et al.* Thermal polymorphism and decomposition of $Y(BH_4)_3$. *Inorg. Chem.* **49**, 3801–3809 (2010).

196. Evans, H. A. *et al.* Polymorphism in $M(H_2PO_2)_3$ (M = V, Al, Ga) compounds with the perovskite-related ReO_3 structure. *Chem. Commun.* **55**, 2964–2967 (2019).

197. Tian, Y.-Q., Zhao, Y.-M., Xu, H.-J. & Chi, C.-Y. CO_2 template synthesis of metal formates with a ReO_3 net. *Inorg. Chem.* **46**, 1612–1616 (2007).

198. Ley, M. B. *et al.* Complex hydrides for hydrogen storage - new perspectives. *Mater. Today* **17**, 122–128 (2014).

199. Mohtadi, R. & Orimo, S.-i. The renaissance of hydrides as energy materials. *Nat. Rev. Mater.* **2**, 16091 (2017).

200. Yan, Y. *et al.* Dehydriding and rehydriding properties of yttrium borohydride $Y(BH_4)_3$ prepared by liquid-phase synthesis. *Int. J. Hydrog. Energy* **34**, 5732–5736 (2009).

201. Olsen, J. E. *et al.* Structure and thermal properties of composites with RE-borohydrides (RE = La, Ce, Pr, Nd, Sm, Eu, Gd, Tb, Er, Yb or Lu) and $LiBH_4$. *RSC Adv.* **4**, 1570–1582 (2014).

202. Ley, M. B., Jørgensen, M., Černý, R., Filinchuk, Y. & Jensen, T. R. From $M(BH_4)_3$ (M = La, Ce) borohydride frameworks to controllable synthesis of porous hydrides and ion conductors. *Inorg. Chem.* **55**, 9748–9756 (2016).

203. Payandeh GharibDoust, S. *et al.* Synthesis, structure, and polymorphic transitions of praseodymium(III) and neodymium(III) borohydride, $Pr(BH_4)_3$ and $Nd(BH_4)_3$. *Dalton Trans.* **47**, 8307–8319 (2018).

204. Grinderslev, J. B., Møller, K. T., Bremholm, M. & Jensen, T. R. Trends in synthesis, crystal structure, and thermal and magnetic properties of rare-earth metal borohydrides. *Inorg. Chem.* **58**, 5503–5517 (2019).

205. Ley, M. B. *et al.* $LiCe(BH_4)_3Cl$, a new lithium-ion conductor and hydrogen storage material with isolated tetranuclear anionic clusters. *Chem. Mater.* **24**, 1654–1663 (2012).

206. Latroche, M. *et al.* Full-cell hydride-based solid-state Li batteries for energy storage. *Int. J. Hydrog. Energy* **44**, 7875–7887 (2019).

207. Maouel, H. A., Alonzo, V., Roisnel, T., Rebbah, H. & Le Fur, E. The first three-dimensional vanadium hypophosphite. *Acta Crystallogr. A* **65**, i36–i38 (2009).

208. Yang, W. *et al.* Carbon nanotube reinforced polylactide/basalt fiber composites containing aluminium hypophosphite: thermal degradation, flame retardancy and mechanical properties. *RSC Adv.* **5**, 105869–105879 (2015).

209. Jain, P., Dalal, N. S., Toby, B. H., Kroto, H. W. & Cheetham, A. K. Order-disorder antiferroelectric phase transition in a hybrid inorganic-organic framework with the perovskite architecture. *J. Am. Chem. Soc.* **130**, 10450–10451 (2008).

210. Jain, P. *et al.* Multiferroic behavior associated with an order-disorder hydrogen bonding transition in metal-organic frameworks (MOFs) with the perovskite ABX_3 architecture. *J. Am. Chem. Soc.* **131**, 13625–13627 (2009).

211. Wang, Z., Hu, K., Gao, S. & Kobayashi, H. Formate-based magnetic metal-organic frameworks templated by protonated amines. *Adv. Mater.* **22**, 1526–1533 (2010).

212. Goldschmidt, V. M. Die gesetze der krystallochemie. *Naturwissenschaften* **14**, 477–485 (1926).

213. Kieslich, G., Sun, S. & Cheetham, A. K. Solid-state principles applied to organic-inorganic perovskites: new tricks for an old dog. *Chem. Sci.* **5**, 4712–4715 (2014).

214. Kieslich, G., Sun, S. & Cheetham, A. K. An extended tolerance factor approach for organicinorganic perovskites. *Chem. Sci.* **6**, 3430–3433 (2015).

215. Seifert, H. On the existence of a vanadium (IV) formate. *J. Inorg. Nuc. Chem.* **27**, 1269–1270 (1965).

216. Paredes-García, V. *et al.* Structural and magnetic characterization of the tridimensional network $[Fe(HCO_2)_3]\bullet nHCO_2H$. *New J. Chem.* **37**, 2120 (2013).

217. Görne, A. L. *et al.* Ammonothermal synthesis, crystal structure, and properties of the ytterbium(II) and ytterbium(III) amides and the first Two rare-earth-metal guanidinates, $YbC(NH)_3$ and $Yb(CN_3H_4)_3$. *Inorg. Chem.* **55**, 6161–6168 (2016).

218. Hu, K.-L., Kurmoo, M., Wang, Z. & Gao, S. Metal-organic perovskites: Synthesis, structures, and magnetic properties of $[C(NH_2)_3][M^{II}(HCOO)_3]$ (M = Mn, Fe, Co, Ni, Cu, and Zn; $C(NH_2)_3$ = guanidinium). *Chemistry - A European Journal* **15**, 12050–12064 (2009).

219. Müller-Buschbaum, K. & Mokaddem, Y. Three-dimensional networks of lanthanide 1,2,4-triazolates: [Yb(Tz)$_3$] and [Eu$_2$(Tz)$_5$(TzH)$_2$], the first 4f networks with complete nitrogen coordination. *Chem. Commun.* 2060–2062 (2006).

220. Rybak, J.-C., Rekawka, A. & Müller-Buschbaum, K. Utilizing a metal melt of gallium for the synthesis of the homoleptic 1,2,4-triazolate dense framework [Ga(Tz)$_3$]. *Z. Anorg. Allg. Chem* **639**, 2382–2385 (2013).

221. Schweinefuß, M. E. *et al.* Indium imidazolate frameworks with differently distorted ReO $_3$-type structures: Syntheses, structures, phase transitions, and crystallization studies. *Cryst. Growth Des.* **14**, 4664–4673 (2014).

222. Abrahams, B. F., Hoskins, B. F., Robson, R. & Slizys, D. A. α-Polonium coordination networks constructed from bis(imidazole) ligands. *Cryst. Eng. Comm.* **4**, 478–482 (2002).

223. Matsumoto, K. *et al.* A peanut-shaped polyaromatic capsule: solvent-dependent transformation and electronic properties of a non-contacted fullerene dimer. *Angew. Chem. Inter. Ed.* **58**, 8463–8467 (2019).

224. Eddaoudi, M. Systematic design of pore size and functionality in isoreticular MOFs and their application in methane storage. *Science* **295**, 469–472 (2002).

225. Yaghi, O. M. *et al.* Reticular synthesis and the design of new materials. *Nature* **423**, 705–714 (2003).

226. Férey, G. Hybrid porous solids: past, present, future. *Chem. Soc. Rev.* **37**, 191–214 (2008).

227. Rosi, N. L., Eddaoudi, M., Kim, J., O'Keeffe, M. & Yaghi, O. M. Advances in the chemistry of metal-organic frameworks. *Cryst. Eng. Comm.* **4**, 401–404 (2002).

228. Deng, H. *et al.* Multiple functional groups of varying ratios in metal-organic frameworks. *Science* **327**, 846–850 (2010).

229. Perry IV, J. J., Perman, J. A. & Zaworotko, M. J. Design and synthesis of metal-organic frameworks using metal-organic polyhedra as supermolecular building blocks. *Chem. Soc. Rev.* **38**, 1400 (2009).

230. Li, J.-R., Timmons, D. J. & Zhou, H.-C. Interconversion between molecular polyhedra and metal-organic frameworks. *J. Am. Chem. Soc.* **131**, 6368–6369 (2009).

231. Gómez-Gualdrón, D. A., Wilmer, C. E., Farha, O. K., Hupp, J. T. & Snurr, R. Q. Exploring the limits of methane storage and delivery in nanoporous materials. *J. Phys. Chem. C* **118**, 6941–6951 (2014).

232. Wilmer, C. E. *et al.* Large-scale screening of hypothetical metalorganic frameworks. *Nat. Chem.* **4**, 83–89 (2012).

233. He, J., Yu, J., Zhang, Y., Pan, Q. & Xu, R. Synthesis, structure, and luminescent property of a heterometallic metal-organic framework constructed from rod-shaped secondary building blocks. *Inorg. Chem.* **44**, 9279–9282 (2005).

234. Henke, S., Schneemann, A., Wütscher, A. & Fischer, R. A. Directing the breathing behavior of pillared-layered metalorganic frameworks via a systematic library of functionalized linkers bearing flexible substituents. *J. Am. Chem. Soc.* **134**, 9464–9474 (2012).

235. Zhu, A.-X. *et al.* Coordination network that reversibly switches between two nonporous polymorphs and a high surface area porous phase. *J. Am. Chem. Soc.* **140**, 15572–15576 (2018).

236. Nowacki, W. Die kristallstruktur von ScF_3. *Z. Kristallogr. Cryst. Mater.* **101**, 273–283 (1939).

237. Drozdov, A. P., Eremets, M. I., Troyan, I. A., Ksenofontov, V. & Shylin, S. I. Conventional superconductivity at 203 kelvin at high pressures in the sulfur hydride system. *Nature* **525**, 73–76 (2015).

238. Duan, D. *et al.* Pressure-induced metallization of dense $(H_2S)_2H_2$ with high-Tc superconductivity. *Sci. Rep.* **4**, 6968 (2015).

239. Einaga, M. *et al.* Crystal structure of the superconducting phase of sulfur hydride. *Nat. Phys.* **12**, 835–838 (2016).

240. Gordon, E. E. *et al.* Structure and composition of the 200 K-superconducting phase of H_2S at ultrahigh pressure: The perovskite $(SH^-)(H_3S^+)$. *Angew. Chem. Int. Ed.* **55**, 3682–3684 (2016). URL http://doi.wiley.com/10.1002/anie.201511347.

241. Majumdar, A., Tse, J. S. & Yao, Y. Mechanism for the structural transformation to the modulated superconducting phase of compressed hydrogen sulfide. *Sci. Rep.* **9**, 5023 (2019). URL http://dx.doi.org/10.1038/s41598-019-41607-1 http://www.nature.com/articles/s41598-019-41607-1.